Retrieving Near-Global Aerosol Loading over Land and Ocean from AVHRR

N. C. Hsu[1,*], J. Lee[1,2], A. M. Sayer[1,3], N. Carletta[1,4], S.-H. Chen[1, 4], C. J. Tucker[1], B. N. Holben[1], and S.-C. Tsay[1]

[1]NASA Goddard Space Flight Center, Greenbelt, MD, USA.

[2]Earth System Science Interdisciplinary Center, University of Maryland, College Park, MD, USA.

[3]Goddard Earth Sciences Technology and Research (GESTAR), Universities Space Research Association, Columbia, MD, USA.

[4]Science Systems and Applications, Inc., Lanham, MD, USA.

*Corresponding author: N. C. Hsu, NASA Goddard Space Flight Center, Greenbelt, MD, USA. (Christina.Hsu@nasa.gov).

Abstract.

The spaceborne Advanced Very High Resolution Radiometer (AVHRR) sensor data record is approaching 40 years, providing a crucial asset for studying long-term trends of aerosol properties regionally and globally. However, due to limitations of its channels' information content, aerosol optical depth (AOD) data from AVHRR over land are still largely lacking. In this paper, we describe a new physics-based algorithm to retrieve aerosol loading over both land and ocean from AVHRR for the first time. The over-land algorithm is an extension of our Sea-viewing Wide Field-of-view Sensor (SeaWiFS) and Moderate Resolution Imaging Spectroradiometer (MODIS) Deep Blue algorithm, while a simplified version of our Satellite Ocean Aerosol Retrieval (SOAR) algorithm is used over ocean. We compare retrieved AVHRR AOD with that from MODIS on a daily and seasonal basis, and find in general good agreement between the two. For the satellites with equatorial crossing times within two hours of solar noon, the spatial coverage of the AVHRR aerosol product is comparable to that of MODIS, except over very bright arid regions (such as the Sahara), where the underlying surface reflectance at 630 nm reaches the critical surface reflectance. Based upon comparisons of the AVHRR AOD against Aerosol Robotic Network (AERONET) data, preliminary results indicate that the expected error confidence interval envelope is around ±(0.03+15%) over ocean and ±(0.05+25%) over land for this first version of the AVHRR aerosol products. Consequently, these new AVHRR aerosol products can contribute important building blocks for constructing a consistent long-term data record for climate studies.

1. Introduction

Success in the quest of quantifying anthropogenic impacts on global change accurately requires decades-long observations of atmospheric, oceanic, and land imaging from space. Analyses of the longest (nearly 40-year) daily record of imager data acquired by the Advanced Very High Resolution Radiometer (AVHRR) aboard the National Oceanic and Atmospheric Administration (NOAA) polar-orbiting meteorological satellites can contribute important building blocks toward this quest. The unique series of AVHRR measurements can be obtained from NOAA-7 (launched in 1981) to NOAA-19 (launched in 2009), comprised of data mainly from two different sensors: the AVHRR/2 instrument that spans from July 1981 to November 2000, followed by the AVHRR/3 to the present. To retrieve aerosol properties from both natural and anthropogenic sources, over both land and ocean, we need to first examine the mechanical, optical, and radiometric characteristics of the AVHRR sensors. These are discussed below.

AVHRR scans mechanically with $\pm 55^{o}$ from nadir and covers a swath width of 2,800 km. Although the native spatial resolution in local area coverage (LAC) mode is 1.1 km at the sub-satellite point, the actual pixel size and shape are somewhat dependent on scan angle. The LAC data are resampled at ~4 km spatial resolution to give a global area coverage (GAC) data set. Within each block of three across-track scan lines by five pixels along-track of LAC pixels, the first four pixels in the first scan line are averaged and the other eleven pixels are skipped. Thus, the AVHRR GAC data are a 4/15 partial sampling of every three by five pixel block, and fifteen being close to the square of four, are often referred to as ‘4 km’ data. The GAC record for a 24-hour period (day and night) totals 0.6 GB, a large volume in the late 1970s but trivial today (Kidwell, 1997).

To fuel the mechanical complexity further, those satellites from NOAA-7 in July 1981 to NOAA-14 in 2000 were permitted to drift in orbit, where the drift or precession was two to three minutes per month in terms of later equatorial crossing times, in turn, introducing artifacts in AVHRR data (Kaufman et al., 2000; Tucker et al., 2005). Our previous results also indicate that this orbital drift imposes significant challenges in determining trends of aerosol loading over land and ocean due to changes in sampling spatial coverage with time (Hsu et al., 2012). Orbital drift was greatly minimized after the launch of NOAA-16 in 2000, and the viewing geometry information for these later sensors is provided within the Level 1 (L1B) input files. Thus, for processing the pre-NOAA K/L/M (or prior to NOAA-15) AVHRR data, we need to calculate the sun-target-sensor geometries directly from the orbital elements of the satellites. The orbital elements, including eccentricity, semi-major axis, inclination, location of ascending node, argument of periapsis, and the anomaly, are obtained from the Two-Line-Elements satellite attitude data source provided by the North American Aerospace Defense Command (*cf.* https://www.celestrak.com/NORAD/documentation/tle-fmt.asp).

The first AVHRR was equipped with four optical channels and was launched in October 1978 on TIROS-N. Subsequently, the sensor was improved to a 5-channel instrument (AVHRR/2, NOAA-7 through 14) and, for the most recent, 6-channel (AVHRR/3, NOAA-15 through 19). These bands are listed in Table 1, and their strengths and limitations for aerosol remote sensing are well-established (*cf.* Tanré et al., 1992; Mischenko et al., 1999 for detailed discussions). In brief, with only two overlapping spectral bands available on most sensors (channels 1 and 2 centered near 630 and 850 nm, *cf.* Figure 1, Table 1), the ability to infer aerosol type is very limited. The spectral width of channel 2 in particular is problematic, since it is a broad band which covers water vapor absorption lines, meaning that ancillary information

about column water vapor content is required to make quantitative use of this band. The AVHRR/3 sensors included a third solar band near 1.6 μm (channel 3a), which improves fine/coarse aerosol discrimination, although this band was inactive on many AVHRR sensors (either the 1.6 μm or 3.7 μm channels were in operation, not both simultaneously), and as such is not considered further at the present time to improve sensor-to-sensor consistency. AVHRR/3 also had the advantage that channels 1 and 2 were narrower and did not significantly overlap compared to the spectral responses of these bands on AVHRR/2 instruments (*cf.* Figure 1). Differences between the sensors' spectral response functions make the task of achieving multi-sensor consistency less straightforward. The remaining three bands (channels 3b, 4, and 5), centered near 3.7, 11, and 12 μm, are more similar between the AVHRR/2 and AVHRR/3 series sensors, and are of great utility for applications such as surface/cloud temperature monitoring and detection of thermally-active aerosols (e.g., mineral dust, volcanic ash). Since AVHRR/1 on TIROS-N and NOAA-6 has only 4 channels and lacks the 12 μm band, which is needed for our Deep Blue algorithm, AVHRR measurements before the year 1981 will not be considered.

Despite these limitations, AVHRR data have been used for retrieving aerosol optical depth (AOD) by various groups. Most AOD data sets created from AVHRR measurements are over-water only, since water surface reflectance in this spectral region is low and can be modeled with reasonable accuracy as a function of near-surface wind speed. One-channel algorithms such as described in Rao et al. (1989) and Stowe et al. (1997) use the 630 nm band (avoiding the difficulties of water vapor absorption in channel 2) but are then restricted to assuming a single aerosol optical model everywhere, which leads to type-dependent AOD biases. Two- or three-channel approaches (e.g., Rao et al., 1989; Mishchenko et al., 1999; Ignatov and Stowe, 2002; Ignatov et al., 2004) permit retrieval of AOD and Ångström exponent (AE), thus providing some

indication of aerosol size, although the sensitivity to size remains small and there is essentially no sensitivity to other parameters such as aerosol absorption. Validation of earlier AVHRR data sets is limited due to the sparse availability of ground-truth data at these times, although a few, mostly regional, studies have been performed (e.g. Stowe et al. 1997, Haywood et al. 2001, Zhao et al. 2002, 2003, 2004). Other studies have focused on more statistical long-term comparisons with Sun photometers rather than instantaneous matchups (Liu et al., 2004), or on comparison of overlapping AVHRR time series to assess sensor-to-sensor consistency (Ignatov et al., 2004).

Several attempts have also been made to use AVHRR to determine AOD over land, for which characterization of land surface reflectance presents a significant difficulty. Knapp and Stowe (2002) proposed a method using Aerosol Robotic Network (AERONET, Holben et al., 1998) to estimate the surface reflectance in the vicinity of individual sites, and then constructing surface reflectance models as a function of land cover type. Riffler et al. (2010) take a 45-day window and essentially use a minimum reflectance technique (with an additional stratification by viewing zenith angle) to estimate surface reflectance for a given location. Mei et al. (2014) used ancillary surface information from the Moderate Resolution Imaging Spectroradiometer (MODIS) in concert with the AVHRR 3.7 μm band (which is comparatively unaffected by the presence of aerosols) and Normalized Difference Vegetation Index (NDVI, Tucker, 1979) to infer surface reflectance over China. In all cases, aerosol optical models are prescribed rather than retrieved, due to the limited information content of the measurements. More recently, synergistic use of AVHRR with other instruments on board the MetOp platforms has enabled improved retrieval of AOD over both land and ocean (EUMETSAT, 2016). The combination of sensors provides additional information content for identification of aerosol type, and

discrimination between clouds and heavy aerosols, which ameliorates some of the issues of AVHRR-only algorithms.

As a result of these obstacles, it has been a highly challenging task to retrieve aerosols globally from AVHRR, particularly over land. Nevertheless, AVHRR instruments provide valuable measurements from 1981 to the present, a time series which is otherwise not available from US Earth Observing System (EOS) sensors. Based upon previous results from our Sea-viewing Wide Field-of-view Sensor (SeaWiFS) Deep Blue aerosol products, we demonstrated that an algorithm based on NDVI using a pair of red and near infrared channels (e.g., 650 and 865 nm, close to AVHRR channels 1 and 2) can be useful in determining surface reflectance over vegetated land when shortwave infrared channels (such as 2.1 μm) are lacking (Hsu et al., 2013). In order to take advantage of this nearly 40-year long-term time series of AVHRR records, we develop a new approach, which is a modified version of the Deep Blue algorithm, to retrieve aerosol properties from AVHRR over land and ocean with similar data structures following the convention of our SeaWiFS aerosol products. Over ocean the Satellite Ocean Aerosol Retrieval (SOAR) algorithm, which has been applied to SeaWiFS and Visible Infrared Imagining Radiometer Suite (VIIRS) measurements (Sayer et al., 2012a, 2017a), is likewise adapted for use with AVHRR to complement Deep Blue by providing coverage over water surfaces. Like SeaWiFS, as AVHRR LAC data are not available everywhere, we use the GAC data in retrieval processing for consistency between satellite platforms.

Sensor radiometric calibration plays a key role in constructing long-term climate data records. This is particularly important for this study, since there is no onboard solar band calibration for AVHRR. Various approaches have been applied to characterize the absolute calibration and on-orbit degradation of the instruments. This first version of the AVHRR Deep

Blue data products uses the calibration of Vermote and Kaufman (1995), which is also used for NASA's long-term NDVI time series data products (e.g. Tucker et al., 2005). Vermote and Kaufman (1995) provide a methodology for the absolute calibration of AVHRR bands 1 and 2, which is repeated through time to monitor and correct for the degradation of these bands on-orbit. A first step uses views of high-altitude bright clouds as 'white' reference targets to provide a relative calibration between the two bands. A second step determines an absolute calibration of channel 1, using off-nadir pixels over ocean where the aerosol load is low and Rayleigh signal comparatively high. This absolute channel 1 calibration can then be transferred to channel 2 using the cloud-derived relative calibration between these bands. Other methodologies have been explored (e.g., Heidinger et al., 2002; Wu et al., 2010; Bhatt et al., 2016), and the use of their calibrations will be investigated for future versions.

In this paper, we describe the details of this new extension of our Deep Blue/SOAR algorithms to AVHRR. Section 2 summarizes the methodology of the over-land and over-water algorithms, and detailed changes made in each key component compared to the other applications of Deep Blue and SOAR. Section 3 illustrates the results of the daily and seasonal aerosol products generated from the new algorithms and their comparisons with those from MODIS. Finally, we show provisional validation of the new AVHRR Deep Blue products in Section 4, followed by some conclusions in Section 5. This paper focuses primarily on the discussion of retrieval algorithms, while a detailed evaluation of the AVHRR Deep Blue aerosol product performance using AERONET and other measurements is provided by a companion paper, Sayer et al. (2017b). In this study, we use data from AVHRR/2 on NOAA-14 and AVHRR/3 on NOAA-18 to demonstrate its capability of processing both older and newer AVHRR instruments, although this algorithm can be applied to other AVHRR sensors from

NOAA-7 to NOAA-19 as well. AVHRR AOD data have been processed using these algorithms for parts of the NOAA-11, NOAA-14, and NOAA-18 missions; more information, including download links, can be found at https://deepblue.gsfc.nasa.gov.

2. Descriptions of AVHRR Aerosol Retrieval Algorithm

To retrieve AVHRR aerosol properties over land and ocean, we employ the Vector LInearized Discrete Ordinate Radiative Transfer (VLIDORT; Spurr, 2006) radiative transfer model to compute the reflected intensity field, which is defined by

$$R(\mu, \mu_0, \varphi) = \frac{\pi I(\mu,\mu_0,\varphi)}{\mu_0 F_0}, \quad (1)$$

where R is the normalized radiance (or apparent reflectance), F_0 is the extra-terrestrial solar flux, I is the radiance at the top of the atmosphere (TOA), μ is the cosine of the view zenith angle, μ_0 is the cosine of the solar zenith angle, and ϕ is the relative azimuth angle between the direction of propagation of scattered radiation and the incident solar direction. This radiative transfer code includes full multiple scattering and takes into account polarization. Using VLIDORT, lookup tables (LUTs) were generated based upon the spectral response functions of a given AVHRR sensor (*cf.* Figure 1) for different solar/viewing geometries and underlying surface (land and ocean) boundary conditions for aerosol retrievals.

However, before the retrieval, the AVHRR TOA reflectances must first be corrected for absorption by ozone, water vapor, and well-mixed gases (details described by Sayer et al., 2017a). For this initial version of the data set, gas absorption coefficients from Ignatov and Stowe (2002) for NOAA-15 were used (since these values are close to average of those reported by that study for NOAA-11, -14, and -18), scaled to account for total column ozone and water vapor read in from the MERRA2 reanalysis (Bosilovich et al., 2015). In addition, for our over-

water retrievals, near-surface wind speed from MERRA2 is used to take into account the effects of oceanic whitecaps and Sun-glint strength adequately, as in prior applications of SOAR (Sayer et al., 2012a, 2017a). After the gas absorption correction, the processing stream is subsequently split into land or ocean algorithm, according to the MODIS land/sea mask, to account for the underlying surface boundary conditions in the LUTs. Advantages of MERRA2 include that it is available for the whole AVHRR record, which enables consistency between processing of different AVHRR sensors, and is at a higher spatial resolution (0.625° longitude, 0.5° latitude) than some other reanalyses.

2.1 Land Algorithm (Deep Blue)

Similar to our SeaWiFS/MODIS algorithm, before the aerosol retrieval is performed, we first screen out the pixels contaminated by the presence of clouds. Due to the lack of the blue bands and 1.38 μm cirrus channel for AVHRR, the previous MODIS cloud screening module has been modified to account for the band differences. The schematic diagram of the AVHRR Deep Blue cloud screening scheme is depicted in Figure 2. We utilize all of the bands that are available for both AVHRR/2 and AVHRR/3 from visible to thermal infrared wavelengths to fully take advantage of the spectral information provided by the AVHRR sensor for detecting clouds. As shown in Figure 2, instead of using the 412 nm channel (available to MODIS and SeaWiFS), a spatial variability filter based on the TOA reflectance at 630 nm (R630) within a 3 × 3 pixel area is employed for AVHRR. Also, in order to account for the dynamic range of surface reflectances at 630 nm over different ecosystem types, different threshold values are applied over darker and brighter surfaces. Based upon our extensive tests, this method is robust in filtering out puffy (e.g. cumulus) clouds as well as cloud edges. Checks on brightness temperature (BT) at 11 μm (BT11) have been implemented in conjunction to BT difference (BTD) between 11 and 12 μm

(BTD11-12) tests to effectively detect high or optically-thin clouds. Finally, in order to distinguish the heavy dust plumes from clouds, we also adopt a heavy dust flag so that the processing stream will bypass the cloud screening module when this is triggered (i.e., BTD11-12 < -1.5 K). These thresholds are empirical, adapted for AVHRR from our prior implementation of Deep Blue to MODIS (e.g. Hsu et al., 2013).

The aerosol optical models used in our AVHRR algorithm are in general consistent with those in the MODIS and SeaWiFS Deep Blue algorithm (*cf.* Hsu et al., 2004, 2013 for details). However, there have been a number of changes made in our AVHRR surface reflectance determination scheme to accommodate the channel differences between AVHRR and SeaWiFS/MODIS. These changes are summarized below.

2.1.1 Determination of Surface Reflectance

As demonstrated in our previous results (Hsu et al., 2013), the calculation of surface reflectance plays a key role in the accuracy of the retrieved aerosol properties. Since AVHRR has limited channels compared to later, more advanced sensors such as SeaWiFS and MODIS, the previous Deep Blue surface reflectance determination scheme needs to be modified. Figure 3 depicts the flowchart of our AVHRR surface reflectance estimation module. The details of each component are described as follows:

2.1.1.1 Deep Blue Surface Database

For urban, dry, and transitional land surfaces, similar to the SeaWiFS/MODIS applications, a database method is used for determining surface reflectance. This was compiled based upon the minimum reflectivity method at 0.1° resolution for each season using AVHRR

TOA reflectance at 630 nm (*cf.* Hsu et al., 2004 for details). In brief, this approach is designed to seek the minimum Rayleigh-corrected TOA reflectance for a certain period of time at each location, and uses this as a proxy for surface reflectance. In order to construct a surface database for AVHRR, we first apply various tests to filter out pixels contaminated by the presence of clouds using cloud screening scheme described above. Reflectances which pass these tests are then corrected for the contribution from molecular (Rayleigh) scattering and averaged into a daily mean for a given grid cell. Finally, the surface reflectance values in the AVHRR database are calculated by a second-order polynomial fit through the lowest 15 percentile of points in a given grid cell against the scattering angles of these observations; the scattering angle (Θ) is defined as

$$\Theta = \cos^{-1}(-\cos\theta_0 \cos\theta + \sin\theta_0 \sin\theta \cos\phi) \quad (2)$$

where θ_0, θ, and ϕ are the solar zenith, sensor view zenith, and relative azimuth angles, respectively. These angular curve fittings of surface reflectance are performed for each NDVI group (NDVI < 0.18, 0.18 ≤ NDVI < 0.35, or NDVI ≥ 0.35) collected in the given grid cell, provided that a sufficient sample size (20 or more points) is acquired. Based on prior experience with SeaWiFS and MODIS, this approach and fit type was found to be able to accurately capture the main angular variations in surface reflectance.

Figure 4 shows the derived global 630 nm surface reflectance maps for NOAA-18 AVHRR, based upon five years (2006-2010) of AVHRR data, for each season using the above approach. Due to limited AVHRR channels and information content the surface database is constructed over both land and ocean in order to help identify the turbid water for the SOAR algorithm (Section 2.2). For the AVHRR over-land algorithm, the surface reflectance is

277 determined using the database approach over moderately bright arid and urban regions where
278 630 nm surface reflectance is between 0.15 and 0.30 (Figure 3). As discussed in e.g. Hsu et al.
279 (2004) and Seidel and Popp (2012), aerosol signals diminish when the surface reflectance
280 reaches the critical surface reflectance; for the 630 nm wavelength this includes many arid and
281 semi-arid regions, such as parts of the Sahara Desert and Arabian Peninsula, as well as snow/ice-
282 covered land. Over these types of surfaces, we cannot accurately retrieve aerosol properties using
283 measurements from single-view satellite sensors with this wavelength. However, 630 nm surface
284 reflectances over arid regions in China and Mongolia are not as bright as those in the Sahara and
285 Arabian Peninsula, and are in general less than 0.30 (Figure 4). Consequently, we exclude pixels
286 over the deserts and semi-deserts in North Africa for retrievals, but include those over dry
287 regions in China and Mongolia where the surface reflectance at 630 nm is below the critical
288 values and thus suitable for aerosol retrievals. Finally, if BTD11-12 is more negative than -1.5 K,
289 AOD retrieval will be performed regardless of surface condition, since for thick dust plumes the
290 majority of the satellite signal comes from atmosphere. Figure 5 shows the geographic regions
291 where different approaches are used for surface reflectance. As described above the database
292 method is used over urban, dry, or transitional land surfaces, while a NDVI method (introduced
293 below) is used over vegetated areas.

294 2.1.1.2 Vegetated Land Surfaces

295 The phenological cycle of vegetation (growth and senescence) means that the reflectance
296 of vegetated surfaces can vary rapidly, particularly compared to barren surfaces such as deserts.
297 Therefore, it is important to determine surface reflectance at a high temporal resolution to
298 minimize errors in AOD related to changing surface characteristics. In this regard, the AVHRRs
299 have a weakness compared to the MODIS and VIIRS sensors, in that the latter two include

shortwave infrared (SWIR) bands, useful for estimating surface characteristics on an instantaneous basis, which AVHRR lacks.

SeaWiFS has a similar limitation. However, based upon our previous SeaWiFS Deep Blue retrievals, we found that the NDVI can serve as a useful proxy to estimate surface reflectance, making it possible to instantaneously derive surface reflectance and thus AOD in both blue (490 nm) and red (670 nm) bands (Hsu et al., 2013; Sayer et al., 2012b). Although the 670 nm AOD showed an AOD-dependent underestimation, the 490 nm AOD, which showed negligible bias, could be used to correct the 670 nm AOD. For AVHRR, our preliminary investigations (not shown) suggested that the NDVI approach resulted in a more significant bias in 630 nm AOD than SeaWiFS. Since there is no additional band in AVHRR to correct for the bias (unlike SeaWiFS), we have developed a modified NDVI-based method to determine surface reflectance for AVHRR, which merge the use of NDVI with the concept of minimum reflectance approach used in our Deep Blue surface database construction mentioned above.

Although similar to the minimum reflectance technique, this method utilizes NDVI rather than TOA reflectance when determining the 'clean' background condition. The Rayleigh-corrected NDVI ($NDVI_{Rc}$) is defined as

$$NDVI_{Rc} = \frac{R_{Rc,band2} - R_{Rc,band1}}{R_{Rc,band2} + R_{Rc,band1}}, \quad (3)$$

where $R_{Rc,band1}$ and $R_{Rc,band2}$ are Rayleigh-corrected TOA reflectances in bands 1 (630 nm) and 2 (850 nm), respectively. The use of NDVI is to avoid extra dimensions for observation geometry when deriving surface reflectance, thereby minimizing the search window. Since the surface reflectance is strongly dependent on observation geometry, the minimum reflectance only represents surface reflectance for the specific observation geometry for which the minimum

reflectance is observed. Figure 6 shows AVHRR Rayleigh-corrected TOA reflectance in band 1 and $NDVI_{Rc}$ for two consecutive orbits on a relatively clean day over the U.S. The $NDVI_{Rc}$ exhibits a much smaller dependence on observation geometry than the Rayleigh-corrected TOA reflectance indicating that 'clean' conditions (i.e. cloud-free, low AOD) can be chosen by compositing only temporal samples for NDVI, in contrast to needing both temporal and angular samples for the TOA reflectance. This is because the ratio in the NDVI definition decreases the angular dependence of the signal.

Consequently, the surface database is created by searching for maximum NDVI (as maximum NDVI corresponds to minimum band 1 surface reflectance) in each 30-day temporal window and 0.1° × 0.1° grid box. The dates of the maximum NDVI are also stored to interpolate (linearly) the NDVI values for the dates in between. The surface reflectance in band 1 ($R_{sfc,band1}$) can then be calculated as

$$R_{sfc,band1} = \frac{1-NDVI_{database}}{1+NDVI_{database}} R_{Rc,band2}, \quad (4)$$

where $NDVI_{database}$ is the maximum NDVI stored in the database. As can be inferred from Eq. (4) the angular dependence of the 630 nm surface reflectance is described by the instantaneous 850 nm TOA reflectance in this approach. Figure 7 shows the 30-day maximum NDVI database created for the year 2006 and four day of year (DOY) windows 1-30, 91-120, 181-210, and 271-300, representative for boreal winter, spring, summer, and fall, respectively. The seasonal variation and spatial pattern of NDVI indicate reliability of a 30-day window. We also investigated (not shown) temporal windows between 10 and 45 days, although neither showed superior performance over the 30-day window in every aspect. Shorter temporal windows tended toward an underestimation in AOD due to the remaining aerosol signal in the NDVI database,

348 while longer temporal windows tended toward overestimation by choosing more densely
349 vegetated conditions than representative for the bulk of the period.

350 Since the NDVI database is susceptible to the residual aerosol signal on the day chosen
351 for the database, an aerosol correction needs to be applied to the database to alleviate the
352 aforementioned underestimation in AOD. To this end, atmospheric correction is performed for
353 AVHRR band 1 and band 2 TOA reflectances to derive atmosphere-corrected (for both Rayleigh
354 and aerosol contributions) NDVI, denoted $NDVI_{Ac}$, and compare with $NDVI_{Rc}$. AVHRR
355 observations are collocated with AERONET sites over North America for the period from 2006
356 to 2011 with a spatial window of 0.1° in latitude and longitude and a temporal window of 30 min.
357 Then, the atmospheric contribution to TOA reflectance is removed using radiative transfer
358 calculations utilizing the AERONET-observed spectral AOD as input. For AERONET, cloud-
359 screened and quality-assured Level 2 direct Sun measurements (Smirnov et al., 2000; Holben et
360 al., 2006) were used, and AOD at AVHRR band 1 and 2 were derived from the spectral AOD
361 and AE over the 440-870 nm wavelength range. The comparison between $NDVI_{Ac}$ and $NDVI_{Rc}$
362 provides useful information for the aerosol correction scheme.

363 Figure 8 shows differences between $NDVI_{Ac}$ and $NDVI_{Rc}$ as a function of 550 nm AOD,
364 $NDVI_{Rc}$, air mass parameter (AMP, $\sec\theta_o \times \sec\theta_v$), and scattering angle, which are factors on
365 which the aerosol signal is dependent. Also shown are the differences after applying corrections
366 for aerosol signals described here. The NDVI differences before the corrections reveal that the
367 aerosol contamination in the $NDVI_{Rc}$ is strongly dependent on AOD and results in negative
368 biases. Relatively weak dependences are also found on NDVI, AMP, and scattering angle. It
369 should be noted that in addition to the strong dependence on AOD, the absolute difference
370 between $NDVI_{Rc}$ and $NDVI_{Ac}$ generally increases with increasing NDVI and decreasing

scattering angle up to ~120°. The dependence on AMP is less significant. This is because both increasing NDVI and decreasing scattering angle enhance the aerosol signal at a given AOD, due to increasing contrast between aerosol and surface signals, and increasing aerosol scattering intensity, respectively. By the same reasoning, a dependence on AMP is also expected (due to increasing aerosol signal with air mass), but the dependence is much smaller than those of the other parameters. This is likely due to the contextual characteristics of the bias and sensitivity.

Trial and error based on the median differences between $NDVI_{Rc}$ and $NDVI_{Ac}$ leads us to the following correction equations:

For scattering angle ≥ 120°,

$$NDVI_{Rc,corrected} = NDVI_{Rc} + [0.23 + 0.15 \times (\mathrm{AMP} - 1)] \times AOD_{550} \times NDVI_{Rc} \quad (5)$$

For scattering angle < 120°,

$$NDVI_{Rc,corrected} = NDVI_{Rc} + [0.23 + 0.15 \times (\mathrm{AMP} - 1) + 0.03 \times (120° - \Theta)] \times AOD_{550} \times NDVI_{Rc} \quad (6)$$

It is found that these corrections significantly improve the medians and central 68% intervals of the NDVI differences (i.e. medians closer to zero and spread of distribution smaller).

In actual implementation, since 'true' background AOD values are not available for each location and time, a monthly AOD climatology (one value for each of the 12 calendar months, not one value for each month of the satellite record) is created using the Aqua MODIS Collection 6 Deep Blue AOD product. Specifically, the 5th percentiles of 13-year Level 3 daily AOD record from 2003 to 2015 in each 1° × 1° grid were chosen to represent the background AOD and used to correct the NDVI database using Eqs. (5) or (6) depending on scattering angle. It should be noted that the climatology was created in a way to correct the NDVI database a marginal amount, such that the different spatial resolution between the NDVI database (0.1°) and AOD

climatology (1°) did not generate a noticeable checkerboard pattern in the spatial distribution of AOD. Likewise, it is expected that the use of a single monthly climatology for the entire AVHRR record would not lead to significant biases. Note that this does not mean that the MODIS Deep Blue record 'feeds in' to the AVHRR record on an instantaneous basis, only to correct the background AOD for the NDVI database calculation as described above. Other aerosol data sets could in principle be used to create this background AOD climatology instead. In this way the actual AVHRR AOD retrieval remains largely independent of the MODIS Deep Blue AOD retrieval.

The performance of the surface reflectances derived from the NDVI database is evaluated by comparing against the atmospherically-corrected TOA reflectances calculated above. Here data with 550 nm AOD from AERONET < 0.2 are only compared to minimize uncertainties in the atmospheric correction procedure. As shown in Figure 9, the NDVI database-derived surface reflectances (estimated surface reflectances) are well-correlated with the atmosphere-corrected TOA reflectances (benchmark surface reflectances) in general, showing root-mean-square error (RMSE) ranging from 1.70% to 2.67% and mean bias (MB) from -0.38% to -0.92% (excluding winter due to the small number of data points). This performance is more than acceptable given the fact that the surface reflectances for AVHRR are from a database at a 30-day temporal resolution rather than instantaneous values (although interpolated between nodes). The outliers (with low number density) are largely due to this temporal limitation of the database approach. These outliers are from a few locations at which the database method is less optimal, and thus would not significantly affect a large-scale view of the aerosol product. For instance, AERONET sites located near croplands, such as Bondville (Illinois, U.S.) and Egbert (Ontario, Canada), and near complex environment, such as Billerica (near Boston, U.S.) contribute to a large portion of

the outliers. It should be noted that in the Level 2 aerosol data product the effect of the outliers, especially due to spatial inhomogeneity, would be mitigated by the spatial aggregation (2 × 2 pixels), as Figure 9 compares data at different spatial resolutions (0.1° for the surface database, L1B resolution for the benchmark).

The application of our NDVI-based land algorithm is limited to certain surface and viewing geometry conditions, due to the use of single 630 nm band in retrieving AOD. Through extensive investigation on retrieval sensitivities and error characteristics of AOD, we have chosen the following procedures to select retrieval pixels for this approach:

i) 630 nm surface reflectance is lower than 0.15, and International Geosphere-Biosphere Programme (IGBP) land cover type (Friedl et al., 2010) is not classified as 'open shrublands', 'grasslands', or 'croplands'. Because AOD retrieval sensitivity decreases with increasing surface reflectance, data are excluded when surface reflectance is too high.

ii) If IGBP land cover type falls into the three categories in i), air mass factor needs to be higher than 2.5 in addition to the surface reflectance criterion for the pixel to be eligible for retrieval. It is found that AOD retrieved over these three land cover types are less accurate compared to that over other land cover types, mainly due to higher surface reflectance values (although less than 0.15) and higher uncertainty of estimating surface reflectance over these regions. This requires the additional filter to only include data with high signal-to-noise ratio, which reduces artificial hotspots resulting from errors in calculated surface reflectance combined with weak aerosol signal.

2.1.2 AOD Determination and Extrapolation to 550 nm

After the surface reflectance is determined based upon surface types as described above, a maximum likelihood method is used with pre-calculated LUTs to match the appropriate values of AOD to the measured reflectances from AVHRR, based on these surface reflectances and the aerosol optical models as used for other satellite sensors (Hsu et al., 2004). This is the same basic approach as used for SeaWiFS/MODIS Deep Blue, except for the different available spectral bands. Note that the 630 nm band is used for the inversion, and thus the retrieved AOD is also at 630 nm. For details of the algorithm see Hsu et al. (2004, 2013).

Since 550 nm AOD is the primary product of the Deep Blue algorithm for other satellite sensors, and is widely used within the aerosol community, the 630 nm AOD is extrapolated to 550 nm using an AE climatology. This saves the data user from having to perform such an extrapolation themselves. The climatology is created from the full Level 2 AERONET record available at the present time. Specifically, multi-year monthly median 440-870 nm AE values at each AERONET site are calculated based on daily median values, when the numbers of data points are higher than 5 for both the daily and monthly calculations. The monthly climatology is then expanded globally to a 1° × 1° grid using exponentially weighted means of the medians from the AERONET sites. For the weighting factor, e-folding lengths of 500 km for longitude and 250 km for latitude are used (to account for prevailing zonal winds over the globe). It was found that the background AOD from AERONET can be accurately interpolated regardless of the e-folding length in the range of 100-1000 km (Zhang et al., 2016), although the error can increase over areas where AERONET sites are sparsely distributed. It should be noted that the single channel retrieval of AVHRR leads us to using a seasonal aerosol optical model in each geographic region rather than retrieving it in each pixel, such that extrapolation of AOD using the optical models is not optimal.

2.2 Ocean Algorithm (SOAR)

The over-water AOD retrieval is based on the same SOAR algorithm applied previously to SeaWiFS and VIIRS observations, simplified to account for the more limited measurement capabilities of the AVHRR sensors. Full details of SOAR are provided by Sayer et al. (2012a, 2017a), and a summary of key points is below.

2.2.1 Selection of Suitable Pixels

Pixels contaminated by Sun-glint, clouds, or suspected of excessively turbid water are excluded from processing; Sun-glint masking is as described in Sayer et al. (2012a) but cloud and turbid water masks are different due to the different spectral bands available to AVHRR. Pixels are identified as cloudy if they are either bright (band 1 TOA reflectance > 0.08), cold (12 μm BT < 270 K), or heterogeneous (3 × 3 pixel standard deviation of TOA reflectance >0.005 for either band 1 or band 2). To minimize contamination from undetected cloud or 3D effects, pixels adjacent to a pixel identified as cloudy are also excluded. These thresholds have been determined empirically and tested to ensure both few false negatives (i.e., undetected cloud) and positives (i.e., over-screening of aerosol plumes).

Pixels are identified as persistently turbid (or potentially land-contaminated) and excluded if the seasonal Deep Blue surface reflectance database value at 630 nm is above 0.06 (Section 2.1.1.1). This typically removes 0-2 pixels on some coastlines, except for areas of larger-scale turbidity such as the Bay of Bengal or mouth of the Amazon River. If such pixels are not excluded then the effect is a positive bias in retrieved AOD, as AVHRR unfortunately has insufficient information content to easily distinguish between turbid water and elevated aerosol loading.

2.2.2 Pixel-Level Retrieval

As with prior applications of SOAR (Sayer et al., 2012a, 2017a), individual pixels are used to retrieve aerosol properties in a multispectral weighted least-squares fit of observed TOA reflectances against pre-computed values stored in LUTs. The SeaWiFS and VIIRS applications simultaneously retrieved the AOD at 550 nm and fine mode fraction (FMF) as well as the best-fit aerosol optical model (which consists of bimodal size distribution parameters and spectral complex refractive index), from which other parameters like AE can be derived in a self-consistent manner. As only two measurements are available for AVHRR, only the AOD and best-fit aerosol optical model are retrieved and the FMF is fixed for each aerosol optical model. The LUT is generated with the VLIDORT radiative transfer code (Spurr, 2006) and aerosol model information is provided in Table 2 (including references for optical model parameters). Use of these models keeps a level of consistency with other applications of SOAR: other over-ocean AOD retrievals for AVHRR typically retrieve AOD and AE but assume the same aerosol size distribution/refractive index globally (e.g., Mishchenko et al., 1999; Ignatov and Stowe, 2002), which is a slightly different approach to aerosol 'typing'. To allow some more flexibility in distinguishing low-AOD conditions between open oceans and continental outflow regions, where FMF may be different (e.g., Smirnov et al., 2011), there are two maritime models with different FMF permitted (but otherwise the same AOD range and modal optical properties). Different LUTs are calculated for each AVHRR sensor, as their central wavelengths and bandwidths are different (e.g., Tanré et al., 1992).

The ocean surface reflectance model used is described in Sayer et al. (2017a), which is an updated version of that from Sayer et al. (2012a), incorporating more recent measurements of optical characteristics of water and pigments. A $\log_{10}$ chlorophyll concentration (mg m^{-3}) of -0.5

510 is assumed, although the surface reflectance over AVHRR bands is only weakly dependent on
511 this over the range of typical oceanic chlorophyll concentrations. As such this approximation
512 should add negligible (<0.01) additional uncertainty in retrieved AOD.

513 The retrieval minimizes the sum of the squared deviation between measurements and
514 LUT values, weighted by assumptions of the uncertainty in the AVHRR bands (from calibration,
515 gas correction, and the forward model), providing essentially a χ^2 statistic referred to as the
516 retrieval cost. At present these relative uncertainties are assumed to be 3% for band 1 and 20%
517 for band 2; this deweighting of band 2 is to account for the greater calibration and gas absorption
518 uncertainties with this band. As a result the AOD is mostly determined by band 1, while band 2
519 provides some constraint on best-fit aerosol optical model. In version 1 of the AVHRR data set,
520 the TOA reflectances have also been scaled for NOAA-14 (by 0.95 and 0.89 for bands 1 and 2)
521 and NOAA-18 (by 0.97 and 0.95) based on validation against AERONET and examination of
522 maps of aerosol model choices. This is an empirical step taken as a first-pass to decrease
523 potential systematic uncertainties related to the sensor calibration used and trace gas absorption,
524 which will hopefully be improved upon for future versions once the different available multi-
525 sensor AVHRR calibrations have been evaluated for aerosol processing. Note that the NASA
526 NDVI products which also use the Vermote and Kaufman (1995) calibration methodology also
527 apply further empirical corrections, although at the NDVI stage rather than the level 1 stage
528 (Tucker et al 2005, and references therein), so such adjustments are not unprecedented.

529 2.3 Aggregation to 2×2 Cell Resolution and Quality Flags

530 Over both land and ocean, after the retrieval, the AOD and other parameters are
531 aggregated to 2×2 ‘cell’ resolution, which is the output resolution for the Level 2 product, and

532 corresponds to approximately 8.8 × 8.8 km^2 horizontal pixel size at the sub-satellite point
533 (although see prior discussion on LAC/GAC sampling). The median of all retrieved quantities is
534 taken (to reduce sensitivity to, e.g., any residual cloud contamination) from the up to 4 available
535 pixels. Over ocean, the aerosol model with the lowest cell-average cost is chosen as the 'best'
536 solution, and this is reported in the Level 2 product. The main retrieved quantity is the AOD at
537 550 nm and AVHRR band 1; over ocean, related information derived from the aerosol optical
538 model (AOD at AVHRR band 2, FMF, and AE) are also provided.

539 Following the convention used in MODIS/SeaWiFS Deep Blue products, the quality
540 assurance (QA) flags in AVHRR Level 2 data also have 4 different levels where QA=0 indicates
541 no retrieval, QA=1 indicates a possible problem with retrieval, and 2/3 indicate moderate and
542 high quality (i.e., no reason to suspect a problem) respectively. Note that over ocean there is no
543 QA=2 category. Over ocean, a cell is assigned QA=3 if the retrieval cost is less than 5 (i.e. a
544 good fit between measurements and forward-modeled reflectances was obtained), at least 2 (out
545 of 4) pixels within the cell were used in the retrieval, and the AOD standard deviation in the cell
546 is less than 1. In practice the requirement for at least 2 out of 4 pixels is the most restrictive. Over
547 land, the AOD standard deviation requirement is stricter (0.35 and 0.20 for QA=2 and 3,
548 respectively), due to the greater difficulty in AOD retrieval over land, and the pixel count
549 requirement is the same as over ocean. Since potentially there still could be cloud contamination
550 in the QA=1 cells, only QA=2 or 3 cells are propagated into Level 3 aggregated data, and in
551 general only QA=2 or 3 retrievals should be used for most applications.

552 ## 3. Results and Discussions

553 Figure 10 illustrates one of the examples of our AVHRR AOD products and its
554 comparison with MODIS Aqua over South America as well as the surrounding water on
555 September 7, 2006. For MODIS, over-land data from the Deep Blue algorithm are used (Hsu et
556 al., 2013; Sayer et al., 2013). Over water, the Dark Target MODIS ocean retrieval product (Tanré
557 et al., 1997; Levy et al., 2013) is used, as SOAR has not yet been applied to MODIS. Our newly
558 developed AVHRR algorithm, shown in Figure 10 (c), extends the spatial coverage of current
559 AVHRR AOD products, which are only available over water, to the land surface types. The
560 AVHRR data shown here are based upon measurements from NOAA-18 with a local solar
561 equator crossing time of ~2:00 pm, which is slightly later than the 1:30 pm equator crossing time
562 for Aqua. Nevertheless, the areas of high AOD in our AVHRR image correspond well to the
563 smoke plumes visible in the MODIS true-color image, capturing the heavy smoke transported
564 southward. We also compare the AOD values at 550 nm derived from our AVHRR data with
565 those based upon the MODIS/Aqua aerosol retrievals for the corresponding day, as shown in
566 Figure 10 (b). The results indicate that the AOD values from these two sensors are quite
567 comparable, despite their differences in observation time.

568 We also examined algorithm results over Asia, which often exhibits the most complex
569 aerosol conditions observed, with a mixture of dust and fine mode pollution particles. One such
570 example, shown in Figure 11, is for April 16, 2006. On this day, a transported dust plume
571 observed over western and central China around 40º N, 80º–114º E occurred as a result of a
572 springtime dust outbreak event over the Taklamakan Desert as well as Inner Mongolia. While
573 this plume was well captured by our AVHRR data, the spatial coverage is sparser over arid
574 regions around 40º N, 80º–105º E compared to the MODIS data. This is due to the use of air
575 mass filter applied to the AVHRR retrievals over arid areas. East of this dust plume, the region

576 was covered by widespread fine mode pollution extending all the way to the East China Sea and
577 the Yellow Sea; the elevated AVHRR AOD values over this area reflect this.

578 In addition to the daily data, we also compare the AVHRR and MODIS products on the
579 seasonal basis. Figure 12 provides the maps of seasonal averaged AOD from both AVHRR
580 (NOAA-18) and MODIS (Aqua). These composites were created by taking daily Level 3
581 products, and then averaging these first to monthly, and then monthly to seasonal, time steps. To
582 stop poorly-sampled grid cells from introducing potentially significant sampling error into the
583 comparison, a daily grid cell was considered valid for an instrument if it contained at least 5
584 retrievals passing QA checks, and a grid cell was considered valid on a monthly basis if it
585 contained at least 3 valid days. These thresholds are somewhat subjective but, particularly for
586 cloudy regions, provide a reasonable balance between data coverage and sampling representivity.

587 As shown in Figure 12, both AVHRR and MODIS reproduce the same major spatial and
588 seasonal variations in aerosol loading. For example, there were intense wild fires over Siberia, in
589 the summer of 2006, producing heavy smoke plumes all the way into the Arctic Ocean, as seen
590 in the retrieved June-July-August AOD maps from both sensors. The patterns of elevated aerosol
591 loading due to anthropogenic air pollution in East Asia and South Asia are also clear in both
592 sensors throughout the year. The seasonal north-south movement of the Saharan dust transport
593 displayed in the AVHRR maps is also in agreement with that in the MODIS maps. More detailed
594 comparisons with the MODIS aerosol products are provided in the companion paper, Sayer et
595 al.(2017b).

596 Seasonal means can be influenced by sampling frequency of the given dataset. AVHRR
597 and MODIS sensors have (to a first order) similar swath widths and similar Level 2 pixel sizes,

598 so it would be expected that sampling frequencies would be similar. Figure 13 confirms that on a
599 general basis this is indeed the case, and also reinforces the extent to which cloud cover,
600 snow/ice, and polar night can limit coverage from all instruments of these types (many grid cells
601 have fewer than 25% of days providing data within a season). Overall AVHRR coverage, while
602 sharing similarities to that of MODIS, is often around 10% less frequent. This is due to the more
603 limited information content of the sensor, meaning that cloud screening and QA checks are
604 stricter in AVHRR to minimize the chances of poor-quality retrievals propagating into the data
605 product. Coverage in the Sahara and Arabian Peninsula is also limited or absent in AVHRR, as
606 this surface is too bright in most cases to perform an AOD retrieval from this type of sensor from
607 the available bands (Section 2.1.1). In AVHRR coverage-sparse regions such as this, sampling
608 differences are also therefore likely to be playing a role in differences in the seasonal AOD
609 observed by the two sensors.

610 Figure 14 shows a comparison of multiannual mean AOD at 550 nm from our NOAA18
611 AVHRR, SeaWiFS (version 4), and MODIS Aqua (Collection 6) aerosol products for their
612 common overlap period (2006-2010). Note the MODIS ocean data are from the standard Dark
613 Target group ocean product (Levy et al., 2013); otherwise, all land data shown are Deep Blue,
614 and ocean data are SOAR. Similar patterns in the mean AOD are seen in all data sets. MODIS
615 has the highest coverage; AVHRR has more gaps due to the sensor's limitations at discerning the
616 aerosol signal over the brightest desert surfaces, as discussed, as well as the more conservative
617 cloud screening (due to more limited spectral channels) reducing coverage over tropical forests.
618 SeaWiFs has similar cloud-screening limitations due to a lack of any thermal IR bands. SeaWiFS
619 also, at this point, represents the oldest of the three Deep Blue algorithm versions and has some
620 additional coverage gaps because of this (Sayer et al. 2012b; Hsu et al. 2013). Some differences

621 in AOD magnitudes result, as in the seasonal comparisons above, from these sampling
622 differences.

623 Over water, the AVHRR and SeaWiFS data are quite comparable. Validation exercises
624 have shown that both have near-zero biases in open-ocean conditions, and slight negative biases
625 in high-AOD conditions (Sayer et al. 2012a, 2017b). Over ocean MODIS shows the same spatial
626 patterns but with a generally higher AOD. As noted, this is not from the SOAR algorithm. The
627 standard MODIS Collection 6 over-ocean AOD product is known to have a positive bias in low-
628 AOD conditions (of order 0.01-0.02; Sayer et al. 2012d, Levy et al. 2013), and a more variable
629 positive bias in dust-laden conditions due to the lack of a non-spherical dust optical model (e.g.
630 Mishchenko et al., 1997, Levy et al., 2003, Banks et al., 2017, Lee et al., 2017). Therefore, these
631 patterns are broadly consistent with the known characteristics of each data set. Additional
632 comparisons are provided in the comparison data set evaluation paper, Sayer et al. (2017b).

633 4. Validation against AERONET AOD

634 Figure 15 shows scatter density plots providing a global summary of the validation of
635 AVHRR retrievals based upon 6 years (2006-2011) of NOAA-18 data and 5 years (1995-1999)
636 of NOAA-14 data over land and ocean. For NOAA-18 a total of 40 sites contributed to over-
637 ocean data, and 427 over land data; for NOAA-14 the numbers are 20 and 123 respectively.
638 Because there are fewer AERONET sites before the year 2000, fewer matchup data points are
639 found for NOAA-14 compared to those for NOAA-18. Full details of the validation are provided
640 by Sayer et al. (2017b), but a summary is given here. AVHRR and AERONET data are
641 compared using the standard technique of averaging satellite data within 25 km of the
642 AERONET site and AERONET data within 30 minutes of the satellite overpass, to decrease the

effect of spatiotemporal sampling differences. The AERONET direct-Sun Version 2 Level 2 (cloud-screened and quality assured; Smirnov et al., 2000) data products are used. This comparison shows results for AVHRR band 1 AOD (near 630 nm). AERONET does not measure this wavelength directly, so the bands are interpolated spectrally, which adds negligible additional uncertainty to the approximate 0.01 AOD uncertainty of the AERONET direct-Sun measurement.

For both NOAA-18 and -14 AVHRR data, the correlation coefficients are high in all cases, and the median biases fairly small. The statistic *f* indicates the fraction of points matching AERONET within the expected error (EE), an envelope of ±(0.03+15%) over ocean and ±(0.05+25%) over land for this first version, on global average for both surface types. While the exact sensitivity to various assumptions is quite dependent on the context of each individual retrieval (i.e. aerosol loading and type, surface cover type, solar/view geometry, etc), these EE envelopes provide a guideline first-order expectation of retrieval performance. They are based on prior applications of the Deep Blue and SOAR algorithms, and the known limitations of the AVHRR sensors (cf. Rao et al., 1989; Tanré et al., 1992; Mishchenko et al., 1999, Hsu et al. 2004, 2013; Sayer et al. 2012a,b, 2017b). Specifically, proportion of retrievals within the expected error calculated separately for regions over ocean, vegetated land only and entire land are 73.9%, 77.0%, and 73.5% (NOAA-18) and 64.3%, 79.4% and 73.9% (NOAA-14), respectively. Uncertainties over ocean are smaller than those over land, due in large part to the darker surface signal. Over land, performance is better when the data are subset to show only vegetated matchups, for the same reason. These results demonstrate the applicability of the Deep Blue and SOAR algorithms to AVHRR measurements.

5. Conclusion

666 To understand the effects of aerosols on climate and human health, satellite observations
667 are crucial in providing continuous temporal and spatial sampling of aerosol properties from
668 source to sink regions for such studies. With the advent of the EOS-era sensors in the late 1990s,
669 an accurate long-term aerosol dataset from these well-calibrated satellite measurements became
670 possible. However, for many climate studies the EOS data records are not always of sufficient
671 length to adequately address the question of long-term aerosol changes on regional/global scales.
672 Therefore, results using earlier satellite sensors such as AVHRR, which provide nearly 40 years
673 of measurements, are highly desirable in order to extend the dataset for use in these studies. This
674 earlier time period (from 1981 to 2000) before the launch of EOS satellites is particularly
675 important for understanding changes in the levels of aerosol loading over Asia, where a large
676 fraction of global economic growth over the past several decades has occurred.

677 In this paper, we demonstrated a new approach to quantitatively retrieve, for the first
678 time, this much needed aerosol information from AVHRR over land and ocean on a global scale.
679 Our approach is an extension of the SeaWiFS/MODIS Deep Blue and SOAR aerosol algorithms.
680 Over land, we merge the use of NDVI with the framework of the minimal reflectance method to
681 account for the effects of changing vegetation in surface reflectance. Over ocean, a simplified
682 version of SOAR is employed for aerosol retrieval. Using these algorithms, our results show that
683 daily, seasonal, and annual distributions of AOD from AVHRR are in reasonable agreement with
684 those from MODIS, despite the limitations on its information content. The cloud screening
685 scheme for AVHRR is also shown to be robust in distinguishing heavy aerosol plumes from
686 clouds, based upon the results of intercomparing daily AOD data from AVHRR and MODIS.

687 Extensive comparisons have also been performed between the AOD values retrieved
688 from the AVHRR instruments on NOAA-14 and -18 and the AERONET data. Using the

689 calibration of Vermote and Kaufman (1995), our AVHRR AOD values show good agreement
690 with the AERONET data over land and ocean for both the NOAA-14 (1995-1999) and NOAA-
691 18 (2006-2011) time periods. Based upon these comparisons, the expected error is estimated to
692 be ±(0.03+15%) over ocean and ±(0.05+25%) over land for this first version of AVHRR aerosol
693 products. Detailed evaluations of the AVHRR products are included in a companion paper
694 (Sayer et al., 2017b). For the next step, we plan to process the AVHRR time series by employing
695 different calibrations (e.g., Heidinger et al., 2002; Wu et al., 2010; Bhatt et al., 2016) to examine
696 the sensor-to-sensor consistency using the multiple overlapping years of data in order to ensure
697 the long-term stability of the aerosol data records.

698 Multiple years of the AVHRR Deep Blue aerosol products from NOAA-11, -14 and -18
699 are now available via the Deep Blue project web site (https://deepblue.gsfc.nasa.gov). This
700 dataset will eventually be able to provide nearly 40 years of aerosol data records from AVHRR
701 not only over ocean, but also over the entire cloud-free, snow/ice-free land area, except for very
702 bright desert regions such as the Sahara and arid regions in the Arabian Peninsula. When
703 combined with data from EOS-era sensors such as SeaWiFS and MODIS, our AVHRR record
704 will provide a critical piece in the construction of a consistent long-term aerosol data record for
705 deriving aerosol trends on both global and regional scales.

706

707 **Acknowledgements**

708 This work was supported by the NASA Radiation Sciences Program, managed by Dr. Hal
709 Maring. The AVHRR Deep Blue data described in this work are freely available to download
710 from https://portal.nccs.nasa.gov/datashare/AVHRRDeepBlue/. Data hosting resources were

711 provided by the NASA High-End Computing (HEC) Program through the NASA Center for
712 Climate Simulation (NCCS) at Goddard Space Flight Center. NOAA L1B GAC data were
713 obtained from https://www.class.ncdc.noaa.gov. MERRA2 data were obtained from NASA's
714 Goddard Earth Sciences Data and Information Services Center (https://disc.gsfc.nasa.gov). We
715 would also like to express our gratitude to AERONET site PIs (https://aeronet.gsfc.nasa.gov) in
716 establishing and maintaining the long-term stations used in this investigation. The authors thank
717 three anonymous reviewers for their helpful suggestions.

718

719 **References**
720
721 Banks, J. R., H. E. Brindley, G. Stenchikov, and K. Schepanski (2017), Satellite retrievals of dust
722 aerosol over the Red Sea and the Persian Gulf (2005–2015), Atmos. Chem. Phys., 17, 3987-
723 4003, doi:10.5194/acp-17-3987-2017.
724
725 Bhatt, R., D. R. Doelling, B. R. Scarino, A. Gopalan, C. O. Haney, P. Minis, and K. M. Bedka
726 (2016), A Consistent AVHRR Visible Calibration Record Based on Multiple Methods
727 Applicable for the NOAA Degrading Orbits. Part I: Methodology, J. Atmos. Ocean Tech., 33,
728 2499–2515, doi:10.1175/JTECH-D-16-0044.1.
729
730 Bosilovich et al. (2015), MERRA-2: Initial Evaluation of the Climate, Technical Report Series
731 on Global Modeling and Data Assimilation, NASA/TM–2015-104606/Vol. 43,
732 https://gmao.gsfc.nasa.gov/pubs/tm/docs/Bosilovich803.pdf [Accessed 08 December 2016].
733
734 Choi, M. J. Kim, J. Lee, M. Kim, Y.-J. Park, U. Jeong, W. Kim, H. Hong, B. Holben, T. F. Eck,
735 C. H. Song, J.-H. Lim, and C.-K. Song (2016), GOCI Yonsei Aerosol Retrieval (YAER)
736 algorithm and validation during the DRAGON-NE Asia 2012 campaign, Atmos. Meas. Tech., 9,
737 1377–1398, doi:10.5194/amt-9-1377-2016.
738
739 EUMETSAT (2016), Polar Multi-Sensor Aerosol Product: User Guide, V2, available online at
740 http://www.eumetsat.int/website/wcm/idc/idcplg?IdcService=GET_FILE&dDocName=PDF_P
741 MAP_PG&RevisionSelectionMethod=LatestReleased [Accessed 17 November 2016].
742
743 Friedl, M. A., D. Sulla-Menashe, B. Tan, A. Schneider, N. Ramankutty, A. Sibley, and X. Huang
744 (2010), MODIS Collection 5 global land cover: Algorithm refinements and characterization
745 of new datasets, Remote Sens. Environ., 114, 168–182, doi:10.1016/j.rse.2009.08.016.
746
747 Haywood, J. M., P.N. Francis, I. Geogdzhayev, M. Mishchenko, and R. Frey (2001),
748 Comparison of Saharan dust aerosol optical depths retrieved using aircraft mounted
749 pyranometers and 2-channel AVHRR algorithms, Geophys. Res. Lett., 28, 2393–2396,
750 doi:10.1029/2000GL012625.
751
752 Heidinger, A. K., C. Cao, and J. T. Sullivan (2002), Using Moderate Resolution Imaging
753 Spectrometer (MODIS) to calibrate advanced very high resolution radiometer reflectance
754 channels, J. Geophys. Res., 107(D23), 4702, doi:10.1029/2001JD002035.
755
756 Holben, B. N., T. F. Eck, I. Slutsker, D. Tanre, J. P. Buis, A. Setzer, E. Vermote, J. A. Reagan,
757 Y. J. Kaufman, T. Nakajima, F. Lavenu, I. Jankowiak, and A. Smirnov (1998), AERONET: A
758 federated instrument network and data archive for aerosol characterization, Remote Sens.
759 Environ., 66, 1–16, doi:10.1016/S0034-4257(98)00031-5.
760
761 Holben, B. N., T. F. Eck, I. Slustker, A. Smirnov, A. Sinyuk, J. Shafer, D. Giles, and O. Dubovik
762 (2006), AERONET's version 2.0 quality assurance criteria, Proc. SPIE, 6408, 64080Q,
763 doi:10.1117/12.706524.
764

765 Hsu, N. C., S. C. Tsay, M. D. King, and J. R. Herman (2004), Aerosol properties over bright-
766 reflecting source regions, IEEE Trans. Geosci. Remote Sens., 42, 557–569, doi:
767 10.1109/TGRS.2004.824067.
768
769 Hsu, N. C., R. Gautam, A. M. Sayer, C. Bettenhausen, C. Li, M. J. Jeong, S.-C. Tsay, and B. N.
770 Holben (2012), Global and regional trends of aerosol optical depth over land and ocean using
771 SeaWiFS measurements from 1997 to 2010, Atmos. Chem. Phys., 12, 8037–8053,
772 doi:10.5194/acp-12-8037-2012.
773
774 Hsu, N. C., M.-J. Jeong, C. Bettenhausen, A. M. Sayer, R. Hansell, C. S. Seftor, J. Huang, and
775 S.-C. Tsay (2013), Enhanced Deep Blue aerosol retrieval algorithm: The second generation, *J.*
776 Geophys. Res. Atmos., 118, doi:10.1002/jgrd.50712.
777
778 Ignatov, A., and L. Stowe (2002), Aerosol Retrievals from Individual AVHRR Channels. Part I:
779 Retrieval Algorithm and Transition from Dave to 6S Radiative Transfer Model, J. Atmos. Sci,
780 59, 313–334, doi: 10.1175/1520-0469(2002)059<0313:ARFIAC>2.0.CO;2.
781
782 Ignatov, A, J. Sapper, S. Cox, I. Laszlo, N. R. Nalli, and K. B. Kidwell (2004), Operational
783 Aerosol Observations (AEROBS) from AVHRR/3 On Board NOAA-KLM Satellites, J. Ocean.
784 Atmos. Tech, 21, 3–26, doi: 10.1175/1520-0426(2004)021<0003:OAOAFO>2.0.CO;2.
785
786 Kaufmann, R.K., Zhou, L., Knyazikhin, Y., Shabanov, N., Myneni, R. and Tucker, C.J. (2000),
787 Effect of orbital drift and sensor changes on the time series of AVHRR vegetation index data.
788 IEEE Transactions on Geoscience and Remote Sensing 38:2584–2597, doi:10.1109/36.885205.
789
790 Kidwell, K.B. (1997). Polar Orbiter Data Users' Guide (TIROS-n, NOAA-6, NOAA-7, NOAA-
791 8, NOAA-9, NOAA-10, NOAA-11, NOAA-12, and NOAA-14). National Oceanic and
792 Atmospheric Administration, Washington, DC.
793
794 Knapp, K. R. and L. L. Stowe (2002), Evaluating the Potential for Retrieving Aerosol Optical
795 Depth over Land from AVHRR Pathfinder Atmosphere Data, J. Atmos. Sci., 59, 279–293, doi:
796 10.1175/1520-0469(2002)059<0279:ETPFRA>2.0.CO;2.
797
798 Lee, J., N. C. Hsu, A. M. Sayer, C. Bettenhausen, and P. Yang, AERONET-based nonspherical
799 dust optical models and effects on the VIIRS Deep Blue/SOAR over-water aerosol product, J.
800 Geophys. Res., submitted.
801
802 Levy, R. C., L. A. Remer, D. Tanré, Y. J. Kaufman, C. Ichoku, B. N. Holben, J. M. Livingston,
803 P. B. Russell, and H. Maring (2003), Evaluation of the Moderate-Resolution Imaging
804 Spectroradiometer (MODIS) retrievals of dust aerosol over the ocean during PRIDE, J. Geophys.
805 Res., 108, 8594, doi:10.1029/2002JD002460, D19.
806
807 Levy, R. C., S. Mattoo, L. A. Munchak, L. A. Remer, A. M. Sayer, F. Patadia, and N. C. Hsu
808 (2013), The Collection 6 MODIS aerosol products over land and ocean, Atmos. Meas. Tech., 6,
809 2989–3034, doi:10.5194/amt-6-2989-2013.
810

811 Liu, L., M. I. Mishchenko, I. Geogdzhayev, A. Smirnov, S. M. Sakerin, D. M. Kabanov, and O.
812 A. Ershov (2004), Global validation of two-channel AVHRR aerosol optical thickness retrievals
813 over the oceans, J. Quant. Spect. Rad. Trans., 88(1-3), 97–109, doi: 10.1016/j.jqsrt.2004.03.031.
814
815 Mei, L. L., Y. Xue, A. A. Kokhanovsky, W. von Hoyningen-Huene, G. de Leeuw, and J. P.
816 Burrows (2014), Retrieval of aerosol optical depth over land surfaces from AVHRR data, Atmos.
817 Meas. Tech., 7, 2411–2420, doi:10.5194/amt-7-2411-2014.
818
819 Mishchenko, M.I., L.D. Travis, R.A. Kahn, and R.A. West, (1997) Modeling phase functions for
820 dustlike tropospheric aerosols using a mixture of randomly oriented polydisperse spheroids. J.
821 Geophys. Res., 102, 16831-16847, doi:10.1029/96JD02110.
822
823 Mishchenko, M . I., I. V. Geogdzhayev, B. Cairns, W. B. Rossow, and A. A. Lacis (1999),
824 Aerosol retrievals over the ocean by use of channels 1 and 2 AVHRR data: sensitivity analysis
825 and preliminary results, Appl. Opt., 38(36), 7325–7341, doi:10.1364/AO.38.007325.
826
827 Rao, C. R. N., L. L. Stowe, and E. P. McClain (1989), Remote sensing of aerosols over the
828 oceans using AVHRR data: Theory, practice and applications, Int. J. Remote Sens., 10(4-5),
829 743–749, doi:10.1080/01431168908903915.
830
831 Riffler, M., C. Popp, A. Hauser, F. Fontana, and S. Wunderle (2010), Validation of a modified
832 AVHRR aerosol optical depth retrieval algorithm over Central Europe, Atmos. Meas. Tech., 3,
833 1255–1270, doi:10.5194/amt-3-1255-2010.
834
835 Sayer, A. M., N. C. Hsu, C. Bettenhausen, Z. Ahmad, B. N. Holben, A. Smirnov, G. E. Thomas,
836 and J. Zhang (2012a), SeaWiFS Ocean Aerosol Retrieval (SOAR): Algorithm, validation, and
837 comparison with other data sets, J. Geophys. Res., 117, D03206, doi:10.1029/2011JD016599.
838
839 Sayer, A. M., Hsu, N. C., Bettenhausen, C., Jeong, M.-J., Holben, B. N., and Zhang (2012b), J.,
840 Global and regional evaluation of over-land spectral aerosol optical depth retrievals from
841 SeaWiFS, *Atmos. Meas. Tech.*, 5, 1761–1778, doi:10.5194/amt-5-1761-2012.
842
843 Sayer, A. M., A. Smirnov, N. C. Hsu, and B. N. Holben (2012c), A pure marine aerosol model,
844 for use in remote sensing applications, J. Geophys. Res., 117, D05213,
845 doi:10.1029/2011JD016689.
846
847 Sayer, A. M., A. Smirnov, N. C. Hsu, L. A. Munchak, and B. N. Holben (2012d), Estimating
848 marine aerosol particle volume and number from Maritime Aerosol Network data, Atmos. Chem.
849 Phys., 12, 8889-8909, doi:10.5194/acp-12-8889-2012.
850
851 Sayer, A. M., N. C. Hsu, C. Bettenhausen, and M.-J. Jeong (2013), Validation and uncertainty
852 estimates for MODIS Collection 6 "Deep Blue" aerosol data, J. Geophys. Res., 118, 7864–7872,
853 doi:10.1002/jgrd.50600.
854
855 Sayer, A. M., Hsu, N. C., Bettenhausen, C., Holz, R. E., Lee, J., Quinn, G., and Veglio, P.
856 (2017a), Cross- calibration of S-NPP VIIRS moderate-resolution reflective solar bands against

857 MODIS Aqua over dark water scenes, Atmos. Meas. Tech., 10, 1425-1444, doi:10.5194/amt-10-
858 1425-2017.
859
860 Sayer, A. M., N. C. Hsu, J. Lee, N. Carletta, S.-H. Chen, and A. Smirnov (2017b), Evaluation of
861 NASA Deep Blue/SOAR aerosol retrieval algorithms applied to AVHRR measurements, J.
862 Geophys. Res., submitted.
863
864 Seidel, F. C. and C. Popp (2012), Critical surface albedo and its implications to aerosol remote
865 sensing, Atmos. Meas. Tech., 5, 1653–1665, doi:10.5194/amt-5-1653-2012.
866
867 Smirnov, A., B. N. Holben, T. F. Eck, O. Dubovik, and I. Slutsker (2000), Cloud screening and
868 quality control algorithms for the AERONET database, Remote Sens. Environ., 73 (3), 337–349,
869 doi: 10.1016/S0034-4257(00)00109-7.
870
871 Smirnov, A., Holben, B. N., Giles, D. M., Slutsker, I., O'Neill, N. T., Eck, T. F., Macke, A.,
872 Croot, P., Courcoux, Y., Sakerin, S. M., Smyth, T. J., Zielinski, T., Zibordi, G., Goes, J. I.,
873 Harvey, M. J., Quinn, P. K., Nelson, N. B., Radionov, V. F., Duarte, C. M., Losno, R., Sciare, J.,
874 Voss, K. J., Kinne, S., Nalli, N. R., Joseph, E., Krishna Moorthy, K., Covert, D. S., Gulev, S. K.,
875 Milinevsky, G., Larouche, P., Belanger, S., Horne, E., Chin, M., Remer, L. A., Kahn, R. A.,
876 Reid, J. S., Schulz, M., Heald, C. L., Zhang, J., Lapina, K., Kleidman, R. G., Griesfeller, J.,
877 Gaitley, B. J., Tan, Q., and Diehl, T. L. (2011), Maritime aerosol network as a component of
878 AERONET – first results and comparison with global aerosol models and satellite retrievals,
879 Atmos. Meas. Tech., 4, 583–597, doi:10.5194/amt-4-583-2011.
880
881 Spurr, R. J. D. (2006), VLIDORT: A linearized pseudo-spherical vector discrete ordinate
882 radiative transfer code for forward model and retrieval studies in multilayer multiple scattering
883 media, J. Quant. Spectros. Radiat. Transfer, 102(2), 316–342, doi:10.1016/j/jqsrt.2006.05.005.
884
885 Stowe, L. L., A. M. Ignatov, and R. R. Singh (1997), Development, validation and potential
886 enhancements to the second generation operational aerosol product at NOAA/NESDIS, J.
887 Geophys. Res., 102 (D14) 16923–16934, doi:10.1029/96JD02132.
888
889 Tanré, D., B. N. Holben, and Y. J. Kaufman (1992), Atmospheric correction algorithm for
890 NOAA-AVHRR products: theory and application, IEEE Trans. Geosci. Remote Sens., 30(2),
891 231–248, doi:10.1109/36.134074.
892
893 Tanré, D., Y. J. Kaufman, M. Herman, and S. Mattoo (1997), Remote sensing of aerosol
894 properties over oceans using the MODIS/EOS spectral radiances, J. Geophys. Res., 102 (D14),
895 16,971–16,988, doi:10.1029/96JD03437.
896
897 Tucker, C. J. (1979), Red and photographic infrared linear combinations for monitoring
898 vegetation, Remote Sens. Environ., 8, 127–150, doi:10.1016/0034-4257(79)90013-0.
899
900 Tucker, C. J., Pinzon, J. E., Brown, M.E., Slayback, D. A., Pak, E. W., Mahoney, R., Vermote,
901 E. R., and N. El Saleous (2005), An extended AVHRR 8-km NDVI dataset compatible with

902 MODIS and SPOT vegetation NDVI data, Int. J. Remote Sens., 26(20):4485–4498,
903 doi:10.1080/01431160500168686.
904
905 Vermote, E. and Y . J. Kaufman (1995), Absolute calibration of AVHRR visible and near-
906 infrared channels using ocean and cloud views, Int. J. Remote Sens., 16(13), 2317–2340,
907 doi:10.1080/01431169508954561.
908
909 Wu, X., J. T. Sullivan, and A. K Heidinger (2010), Operational calibration of the Advanced Very
910 High Resolution Radiometer (AVHRR) visible and near-infrared channels, Can. J. Remote Sens.,
911 36(5), 602–616, doi:10.5589/m10-080.
912
913 Yoon, J. M., J. Kim, J. H. Lee, H. K. Cho, B. J. Sohn, and M. H. Ahn (2007), Retrieval of
914 aerosol optical depth over East Asia from a geostationary satellite, MTSAT-1R, Asia-Pac, J.
915 Atmos. Sci., 43, 133–142, doi:10.1063/1.3116999.
916
917 Zhang, H., S. Kondragunta, I. Laszlo, H. Liu, L. A. Remer, J. Huang, S. Superczynski, and P.
918 Ciren (2016), An enhanced VIIRS aerosol optical thickness (AOT) retrieval algorithm over land
919 using a global surface reflectance ratio database, J. Geophys. Res. Atmos., 121, 10,717–10,738,
920 doi:10.1002/2016JD024859.
921
922 Zhao, X., L. L. Stowe, A. Smirnov, D. Crosby, J. Sapper, and C. R. McClain (2002),
923 Development of a global validation package for satellite oceanic aerosol optical thickness
924 retrieval based on AERONET observations and its application to NOAA/NESDIS operational
925 aerosol retrievals, J. Atmos. Sci., 59, 294–312, doi:10.1175/1520-
926 0469(2002)059<0294:DOAGVP>2.0.CO;2.
927
928 Zhao, T. X.-P., I. Laszlo, O. Dubovik, B. N. Holben, J. Sapper, D. Tanré, and C. Pietras (2003),
929 A study of the effect of non-spherical dust particles on the AVHRR aerosol optical thickness
930 retrievals, Geophys. Res. Lett., 30, 1317, doi:10.1029/2002GL016379.
931
932 Zhao, T. X.-P., O. Dubovik, A. Smirnov, B. N. Holben, J. Sapper, C. Pietras, K. J. Voss, and R.
933 Frouin (2004), Regional evaluation of an advanced very high resolution radiometer (AVHRR)
934 two-channel aerosol retrieval algorithm, J. Geophys. Res., 109, D02204,
935 doi:10.1029/2003JD003817.
936
937
938
939

940
941 Table 1. AVHRR channel names, approximate ranges of peak spectral response, and shorthand
942 for central wavelengths indicated in this study. Note channel 3A is only present on the
943 AVHRR/3 sensors (NOAA15 onwards).

944

Number	Range of peak spectral response (μm)	Shorthand
1	0.58-0.68	630 nm
2	0.72-1.0	850 nm
3a	1.58-1.64	1.6 μm
3b	3.55-3.93	3.7 μm
4	10.30-11.30	11 μm
5	11.50-12.50	12 μm

945

946

947

948 Table 2. Aerosol optical model, AOD ranges, FMF values, size distribution parameters,
949 refractive indices, and references for the AVHRR application of SOAR. For each model fine
950 mode parameters are on the first line and coarse the second.

Model	Reference	FMF	AOD range	Modal radius, μm	Spread	Refractive index (550, 630, 840 nm)
Dust	Lee et al (2017)	0.1	0.15-5.0	0.19	0.44	1.430-0.001*i*, 1.430-0.001*i*, 1.430-0.001*i*
				2.0	0.51	1.543-0.0012*i*, 1.543-0.0009*i*, 1.521-0.0006*i*
Fine-dominated	Sayer et al (2012a)	0.8	0.2-3.5	0.19	0.44	1.430-0.0075*i*, 1.430-0.0075*i*, 1.430-0.0075*i*
				2.75	0.65	1.363-0*i*, 1.363-0*i*, 1.363-0*i*
Marine, 1	Sayer et al (2012a,c)	0.5	0.001-0.2	0.157	0.5	1.414-0.0021*i*, 1.413-0.0025*i*, 1.408-0.0035*i*
				2.59	0.72	1.361-0*i*, 1.358-0*i*, 1.357-0*i*
Marine, 2	Sayer et al (2012a,c)	0.7	0.001-0.2	0.157	0.5	1.414-0.0021*i*, 1.413-0.0025*i*, 1.408-0.0035*i*
				2.59	0.72	1.361-0*i*, 1.358-0*i*, 1.357-0*i*

951

952

953

954

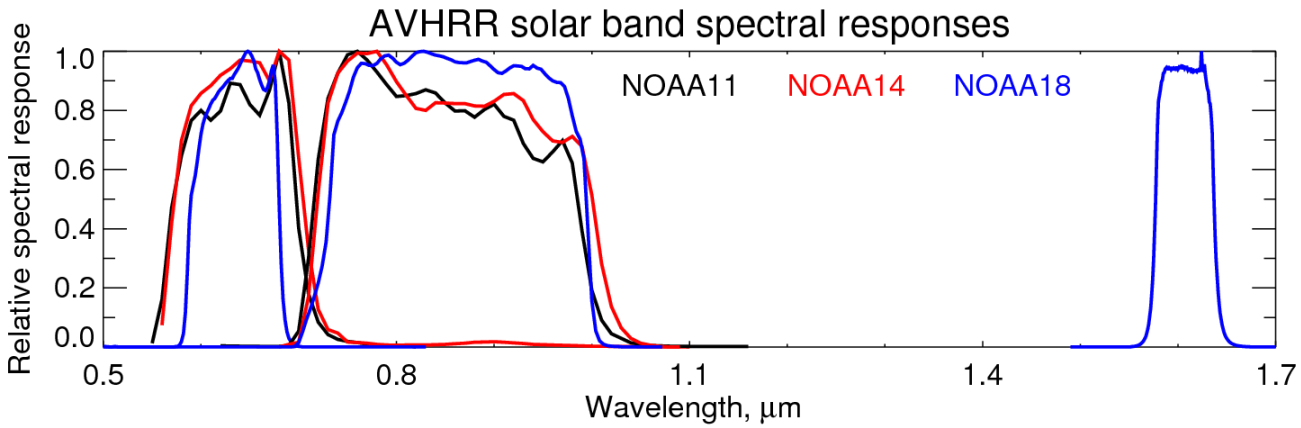

955

956 Figure 1. Solar band spectral response functions for AVHRR/2 on NOAA11 (black), NOAA14 (red), and

957 AVHRR/3 on NOAA18 (blue). Spectral response functions are available from

958 https://www.star.nesdis.noaa.gov/smcd/spb/fwu/homepage/AVHRR/spec_resp_func/index.html .

959

960

961

962

963

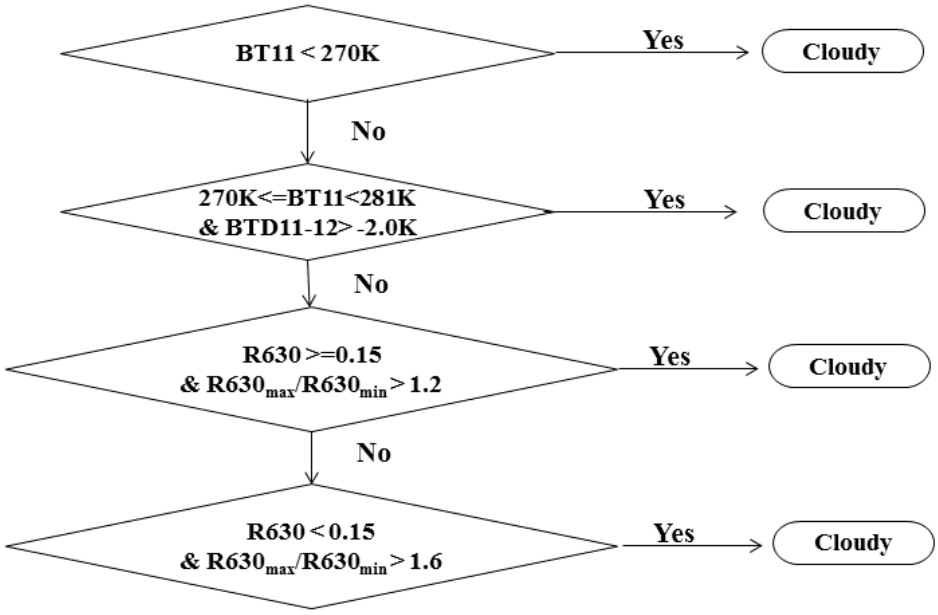

964

965 Figure 2. Schematic diagram of cloud screening scheme used in the AVHHR Deep Blue over-land
966 algorithm. Acronyms indicate brightness temperatures (BT), BT differences (BTD), and reflectances (R)
967 at channel wavelengths denoted. Subscripts max and min refer to the maximum and minimum values
968 within the 3x3 pixel area.

969

970

971

972

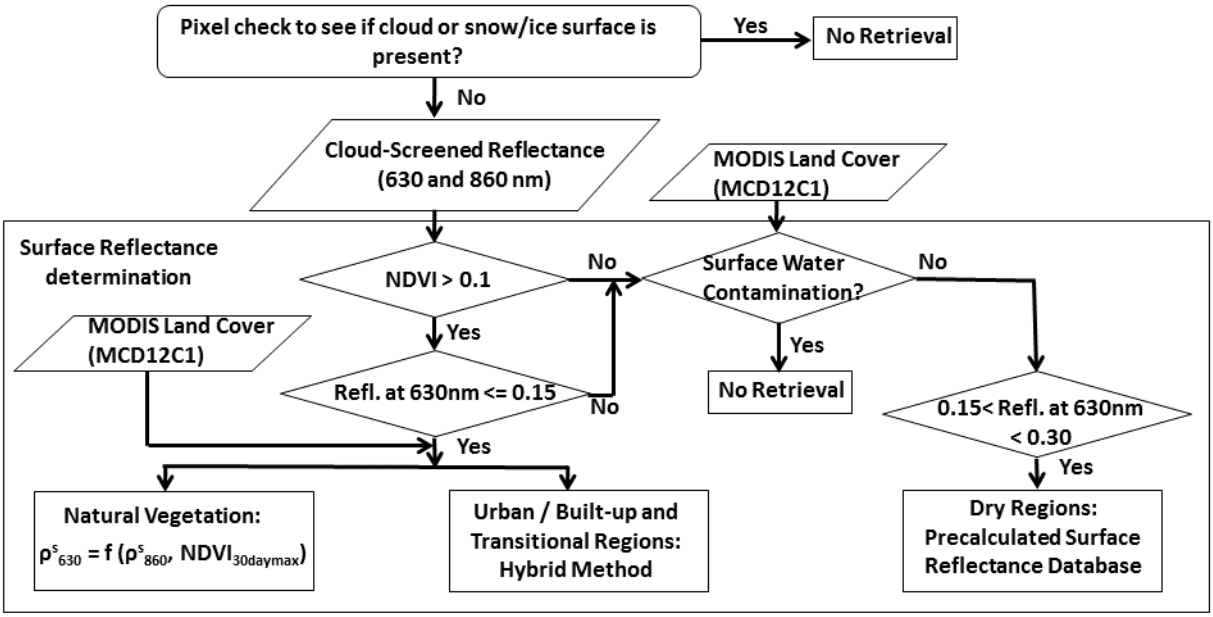

973

974 Figure 3. Flowchart of the AVHRR Deep Blue land surface reflectance determination scheme.

975

976

977

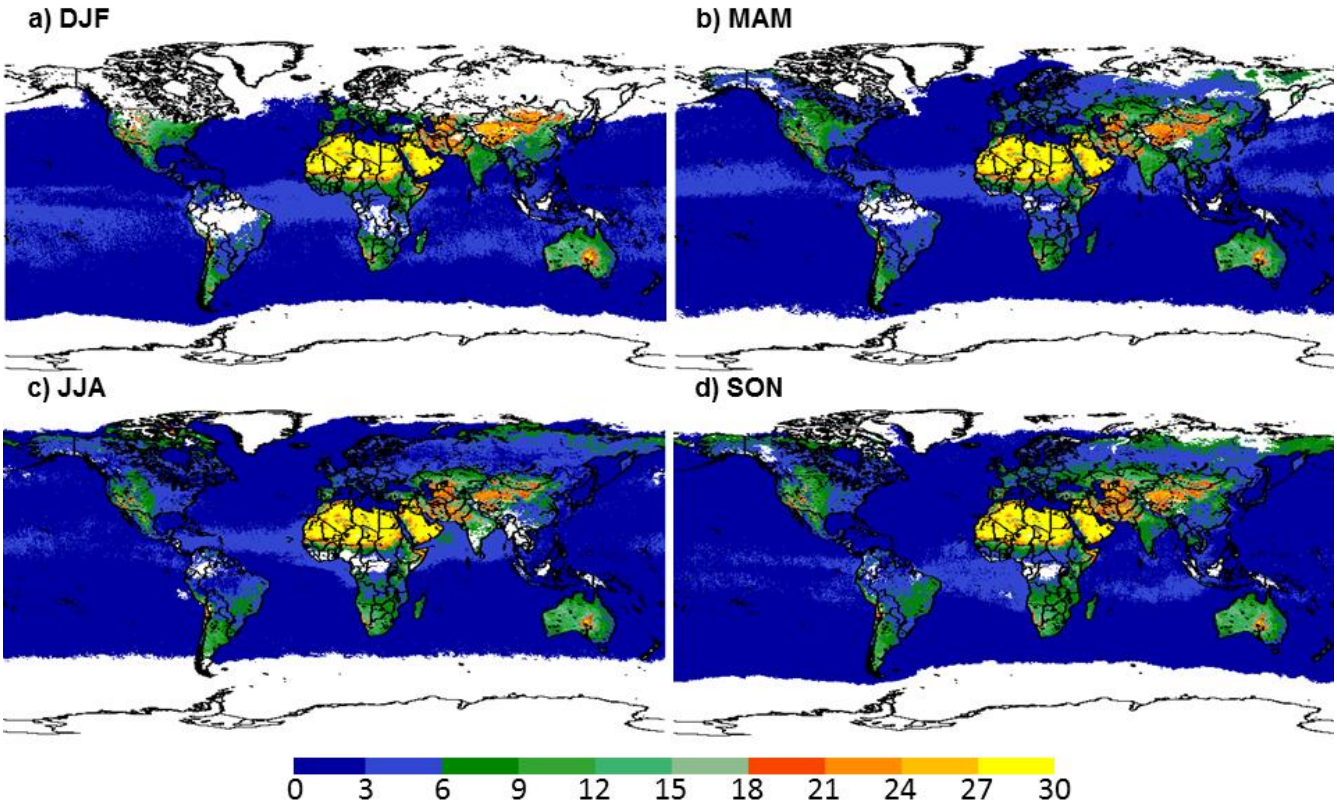

Figure 4. Seasonal maps of NOAA-18 AVHRR surface database showing reflectance (%) at band 1 (630 nm) for (a) December-February, (b) March-May, (c) June-August, and (d) September-November. Grid cells without a valid value are indicated in white.

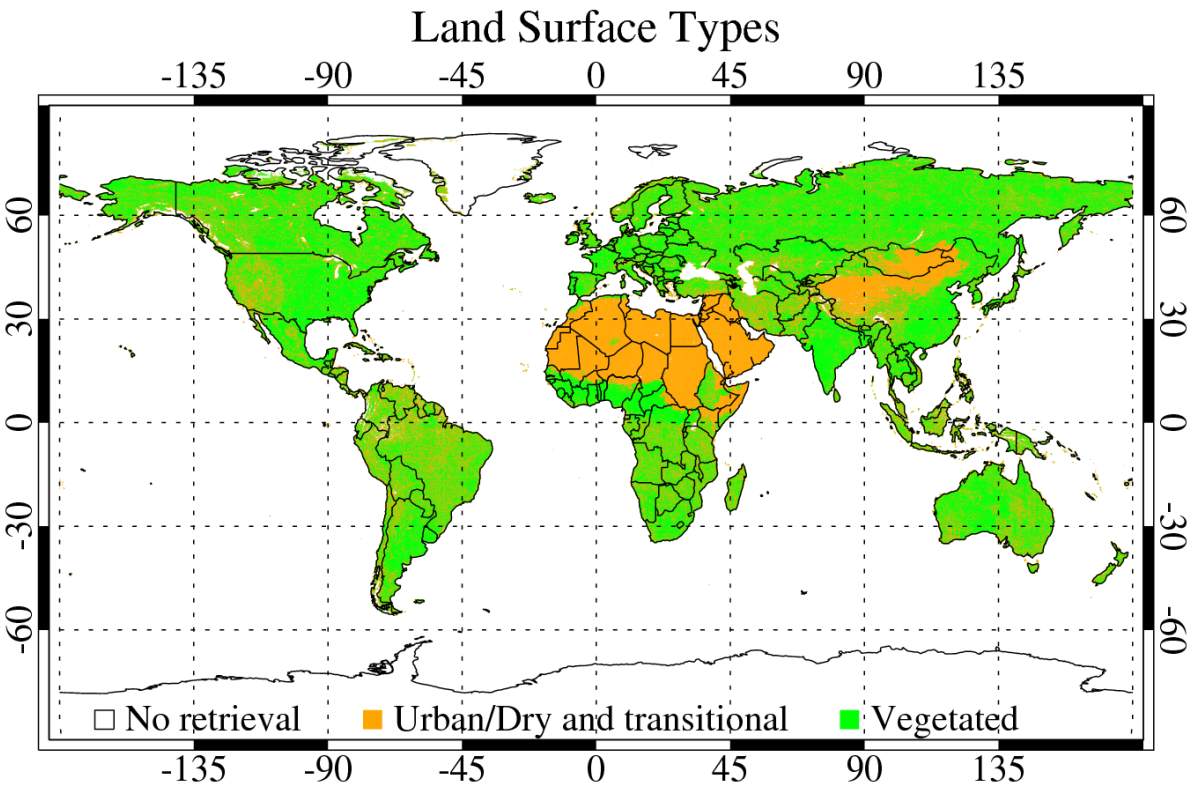

983

984 Figure 5. Land surface types showing where each surface reflectance approach is applied. The seasonal
985 surface reflectance database with scattering angle dependence is used for urban, dry, or transitional land
986 surfaces (orange), and 30-day maximum NDVI database is used for vegetated surfaces (green).

987

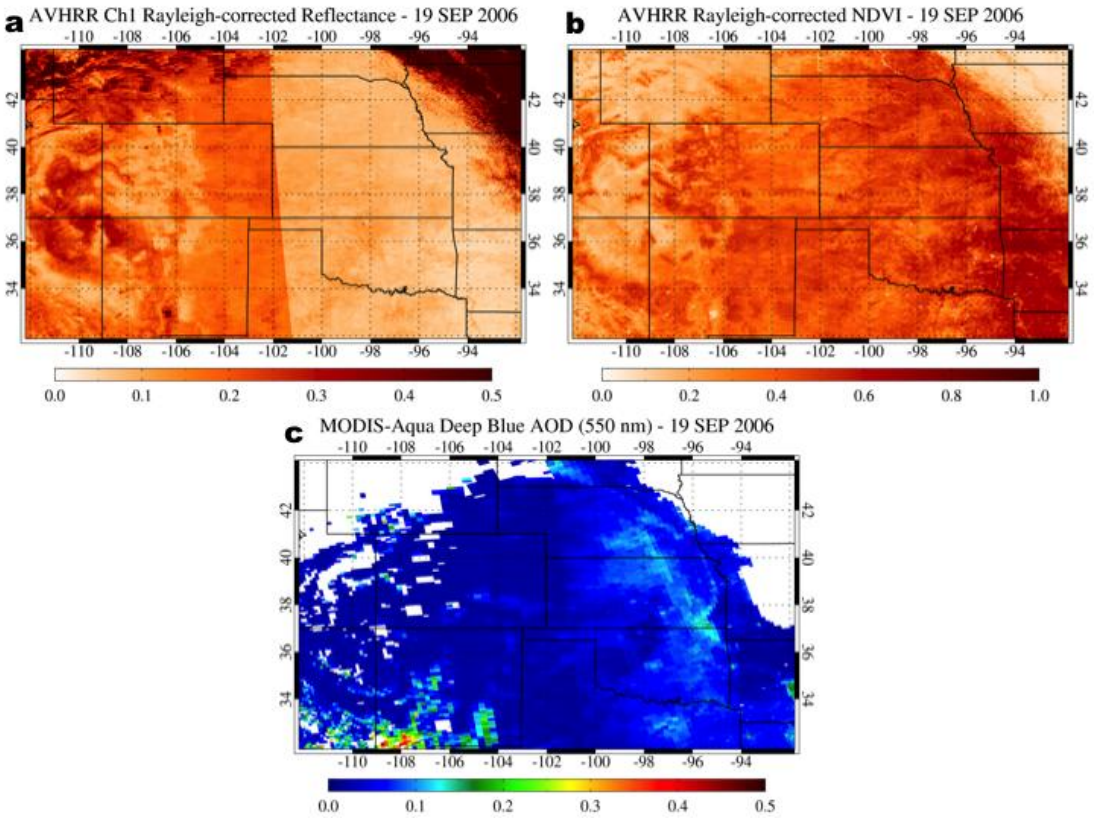

988

989 Figure 6. (a) AVHRR band 1 (630 nm) Rayleigh-corrected TOA reflectance, and (b) Rayleigh-corrected

990 NDVI, and (c) MODIS Aqua Deep Blue AOD at 550 nm over part of the U.S. on 19 September 2006.

991

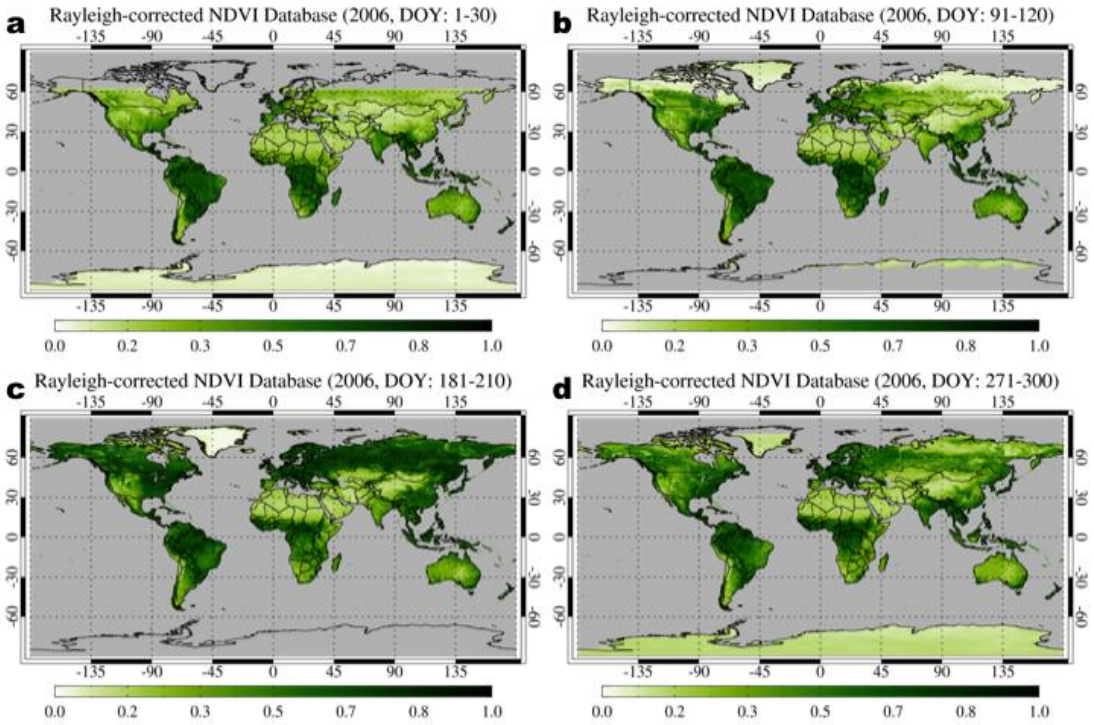

Figure 7. Maximum Rayleigh-corrected NDVI in four 30-day windows in 2006. Day of year windows for each plot are (a) 1-30, (b) 91-120, (c) 181-210, and (d) 271-300, representative of boreal winter, spring, summer, and fall respectively.

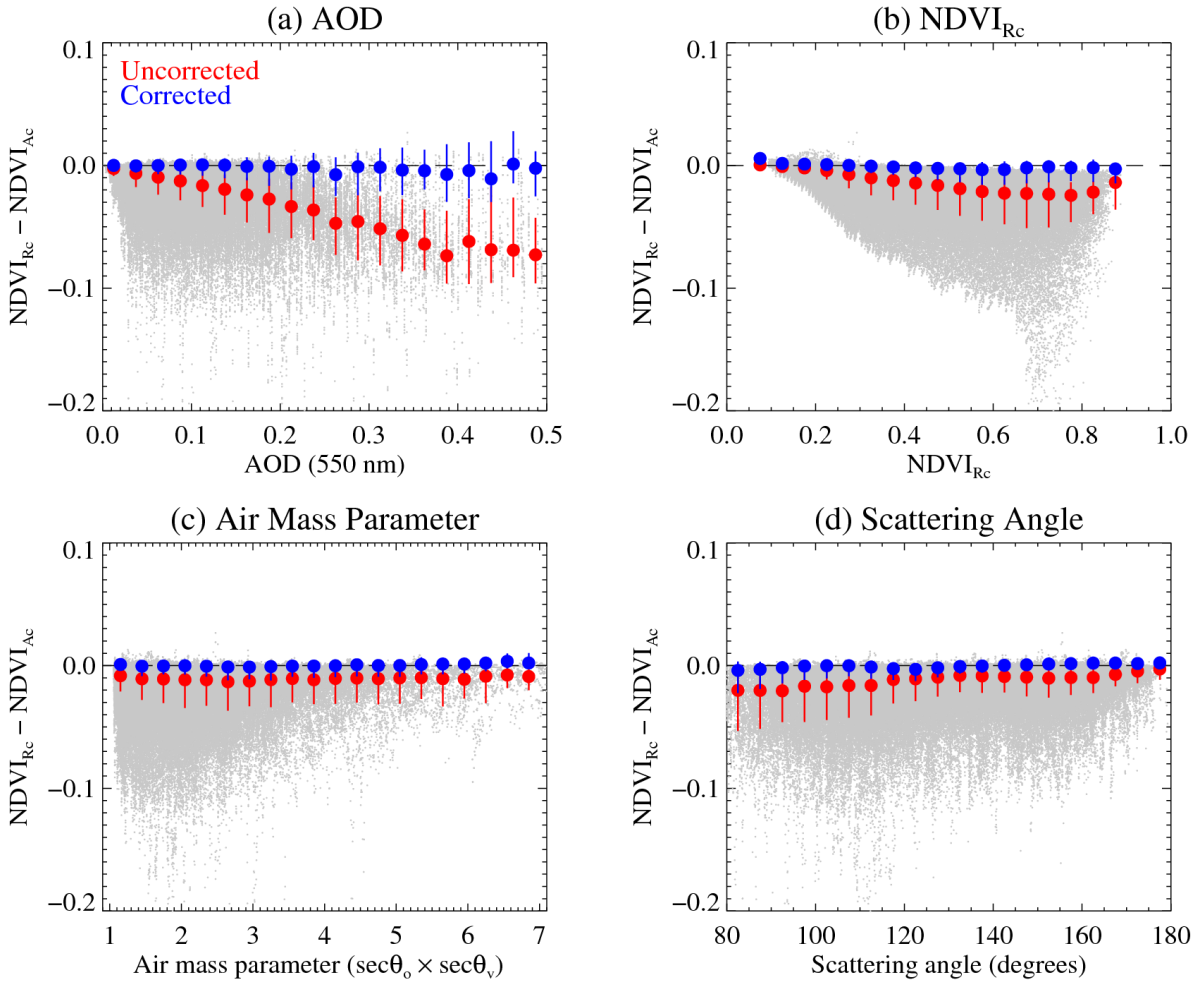

997

998 Figure 8. Median and central 68% interval of the difference between Rayleigh-corrected NDVI ($NDVI_{Rc}$)
999 and atmosphere-corrected NDVI ($NDVI_{Ac}$) as a function of (a) 550 nm AOD, (b) $NDVI_{Rc}$, (c) air mass
1000 parameter, and (d) scattering angle for the period from 2006 to 2011 before (red) and after (blue) the
1001 correction of aerosol signals in $NDVI_{Rc}$. Gray dots show individual data points used for the uncorrected
1002 data. All North American AERONET sites available for the test period are used for this analysis.

1003

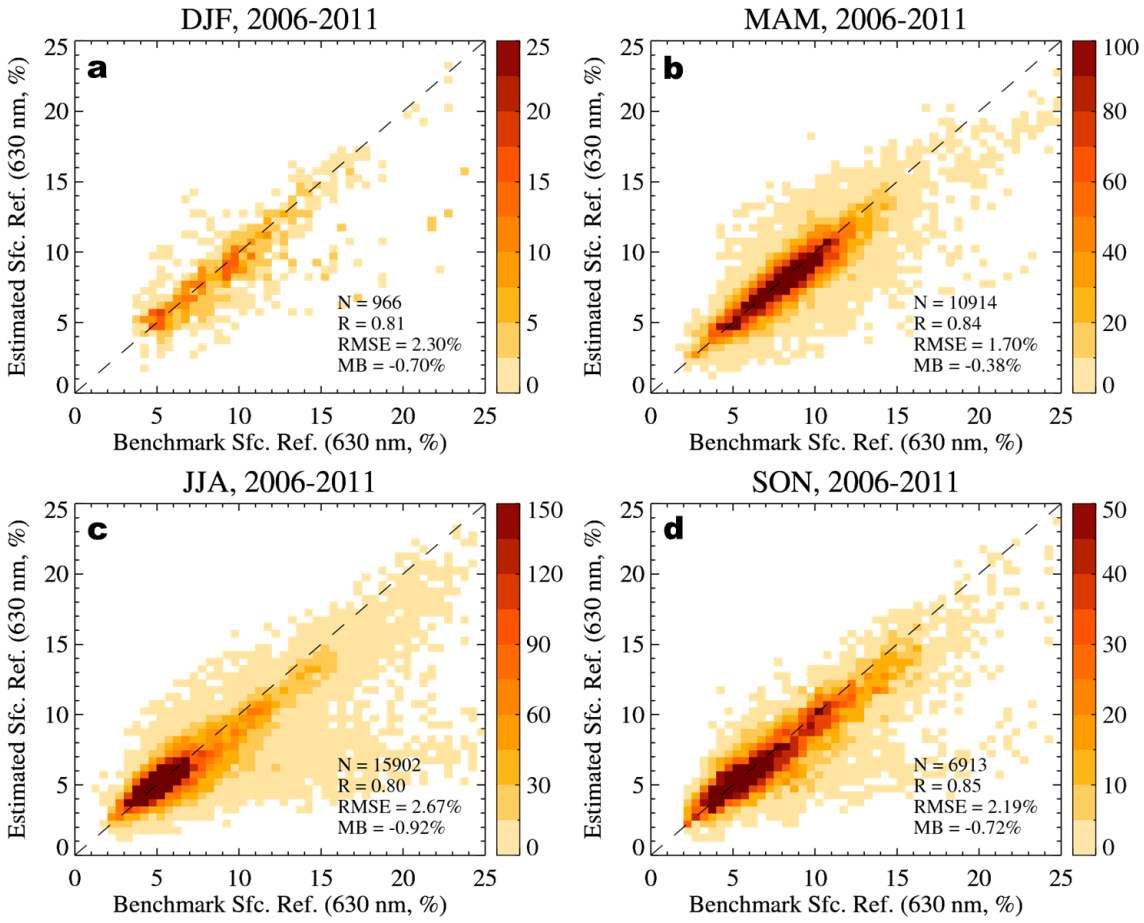

1004

1005 Figure 9. Scatter density plots between benchmark surface reflectance (atmospherically-corrected TOA
1006 reflectance) and estimated surface reflectance from the maximum NDVI database over North America in
1007 each season from 2006 to 2011. Statistics shown are the number of data points (N), Pearson coefficient
1008 (R), root-mean-square error (RMSE), and mean bias (MB).

1009

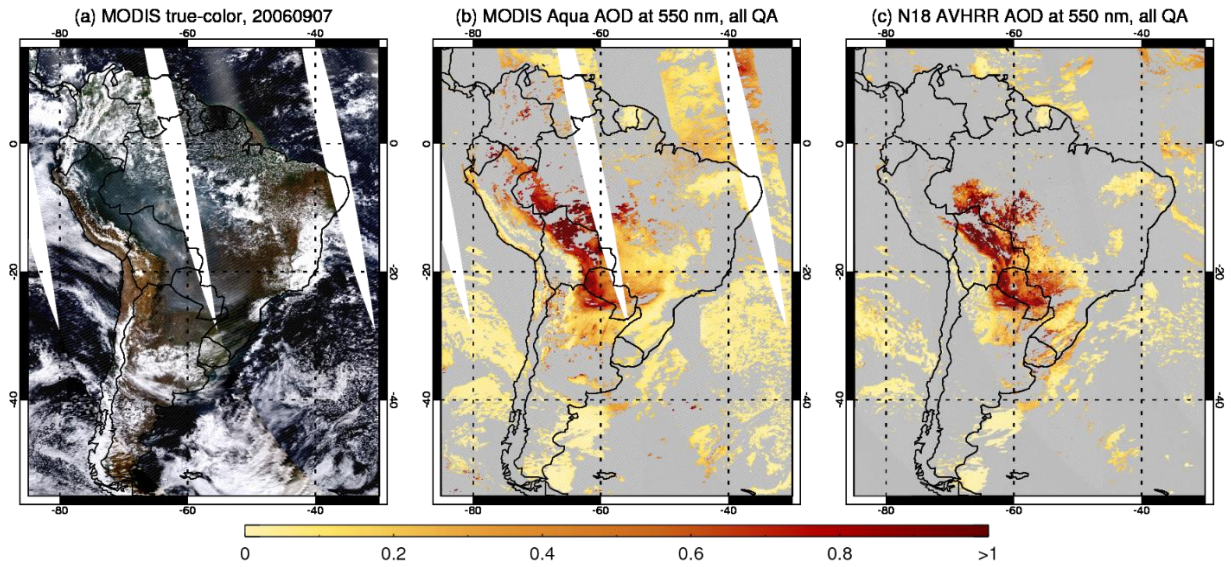

1010

1011 Figure 10. (a) MODIS Aqua true-color image, (b) MODIS AOD at 550 nm from Collection 6, and (c) the

1012 new AVHRR AOD at the same wavelength from NOAA18, for a smoke event over South America on 7

1013 September 2006.

1014

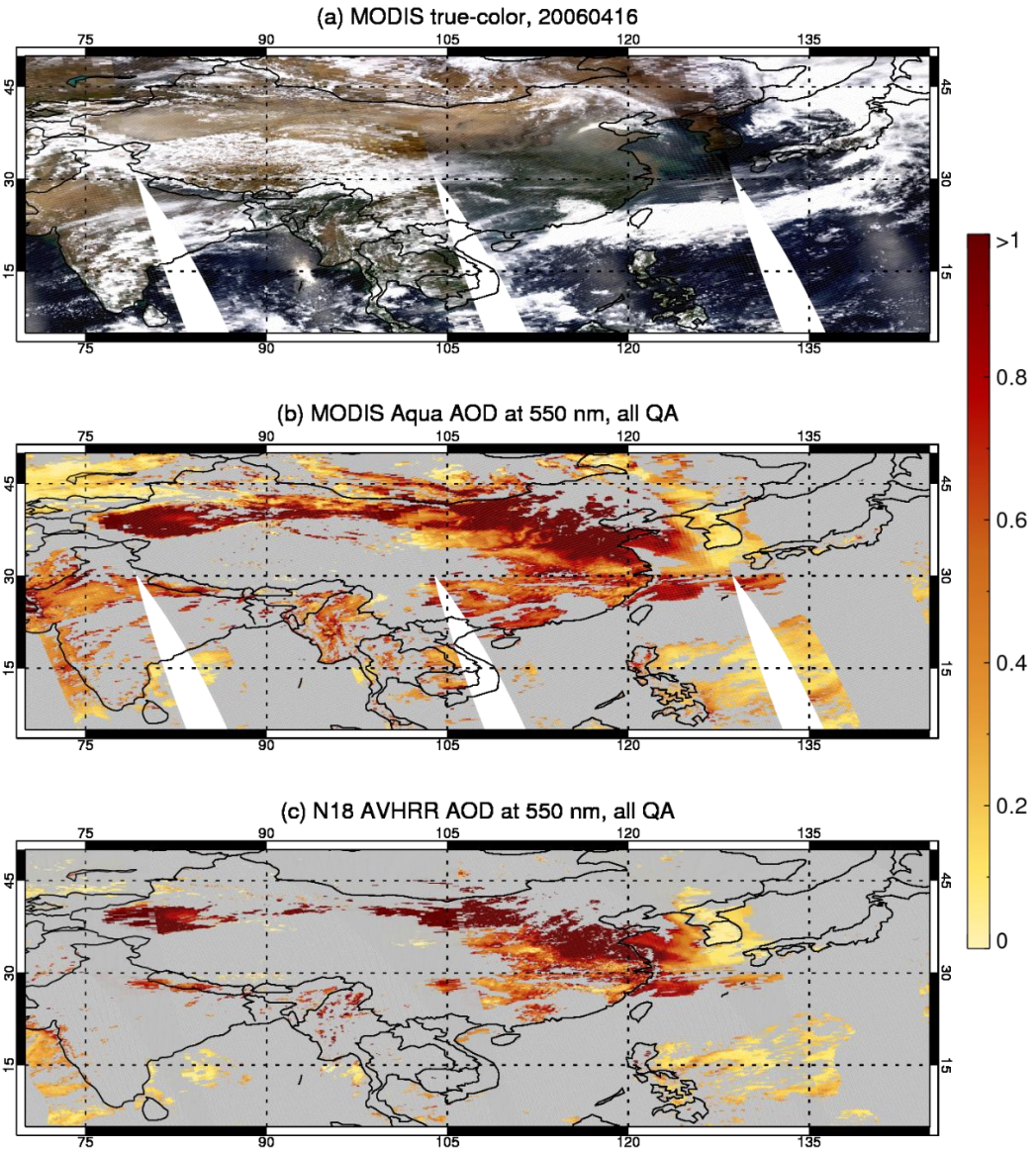

Figure 11. As Figure 10, except for a heavy dust/pollution mixture event over Asia on 16 April 2006.

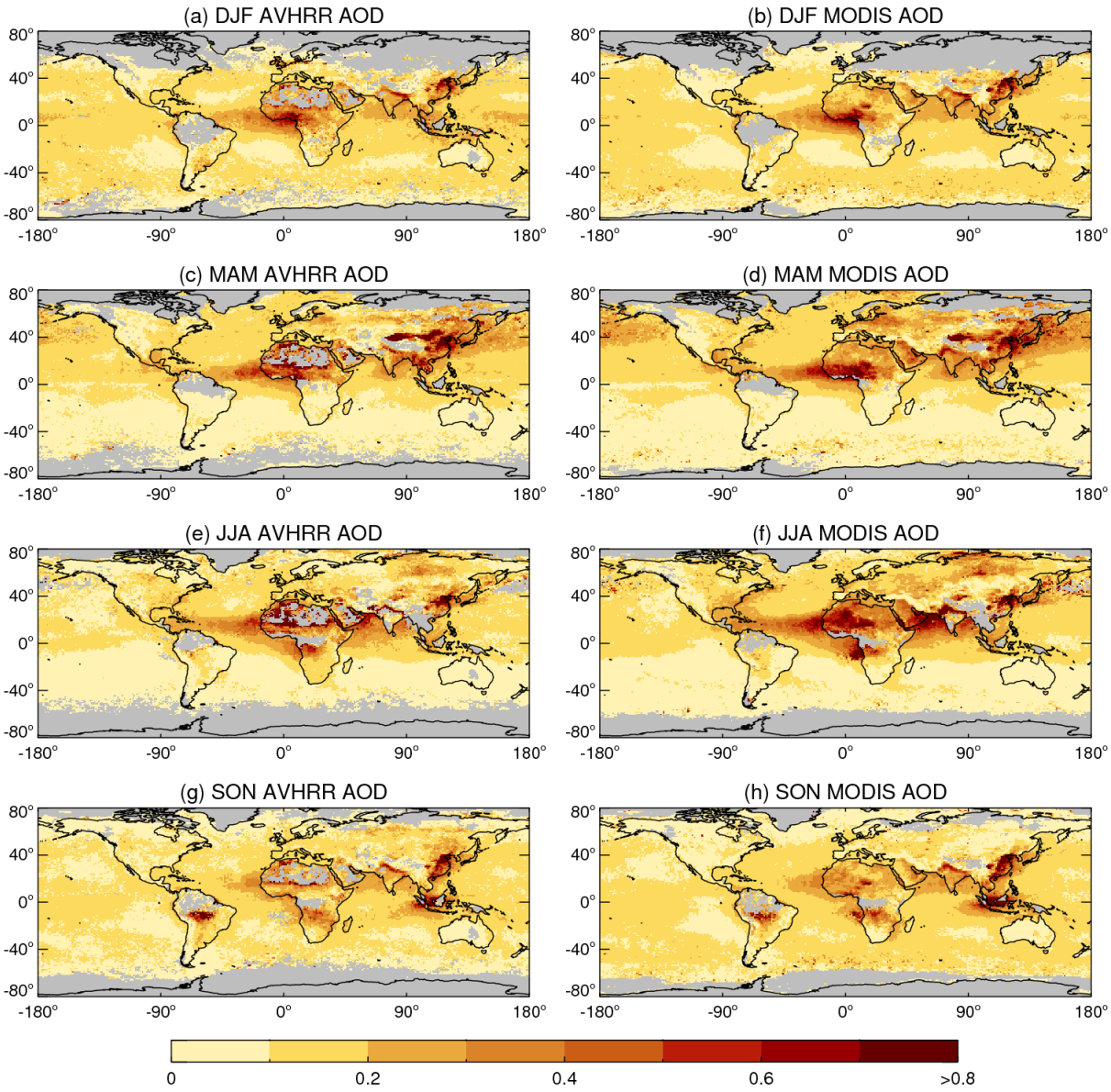

1022

1023

1024 Figure 12. Seasonal composites of NOAA-18 AVHRR (left) and MODIS Aqua (right) AOD at

1025 550 nm for the year 2006. Grid cells without sufficient data (see text) are shaded in grey.

1026

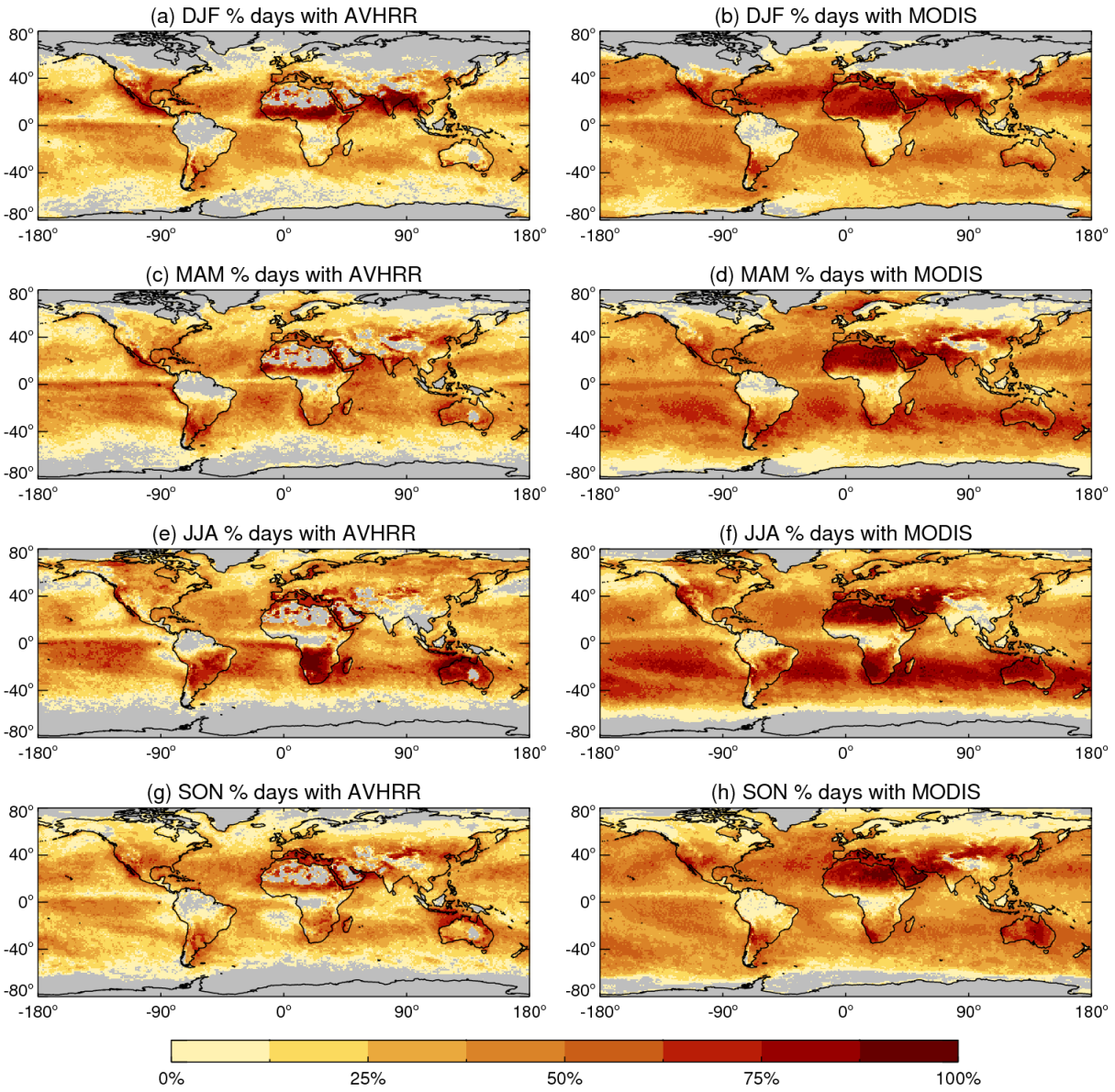

Figure 13. As Figure 12, except for showing the percentage of days within each season containing sufficient AOD data for the Level 3 grid cells to be populated (see text).

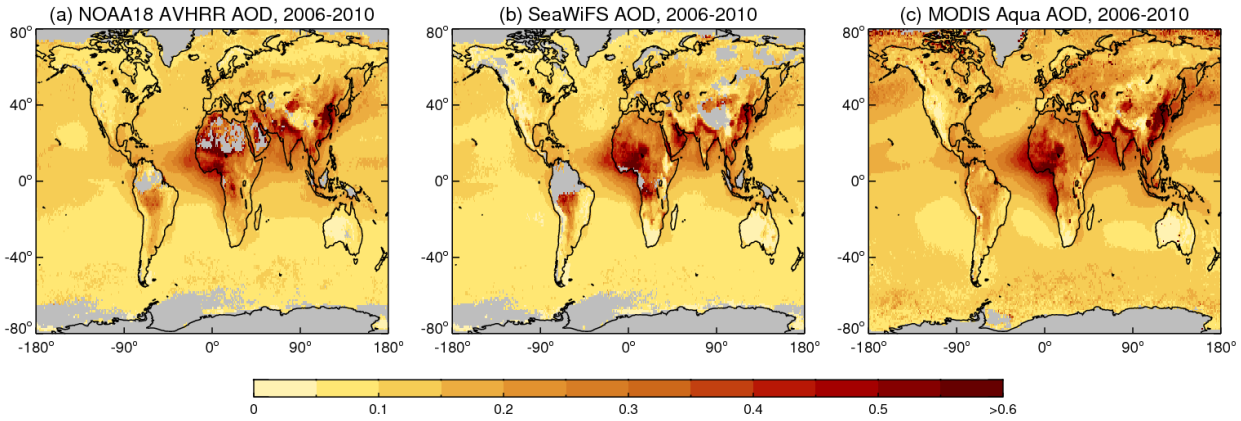

1036

1037 Figure 14. Multiannual mean composites of AOD at 550 nm, for (a) NOAA18 AVHRR, (b)

1038 SeaWiFS, and (c) MODIS Aqua, for their common overlap period (2006-2010). Grid cells with

1039 fewer than 24 months during this period containing valid monthly mean data are shaded in grey.

1040

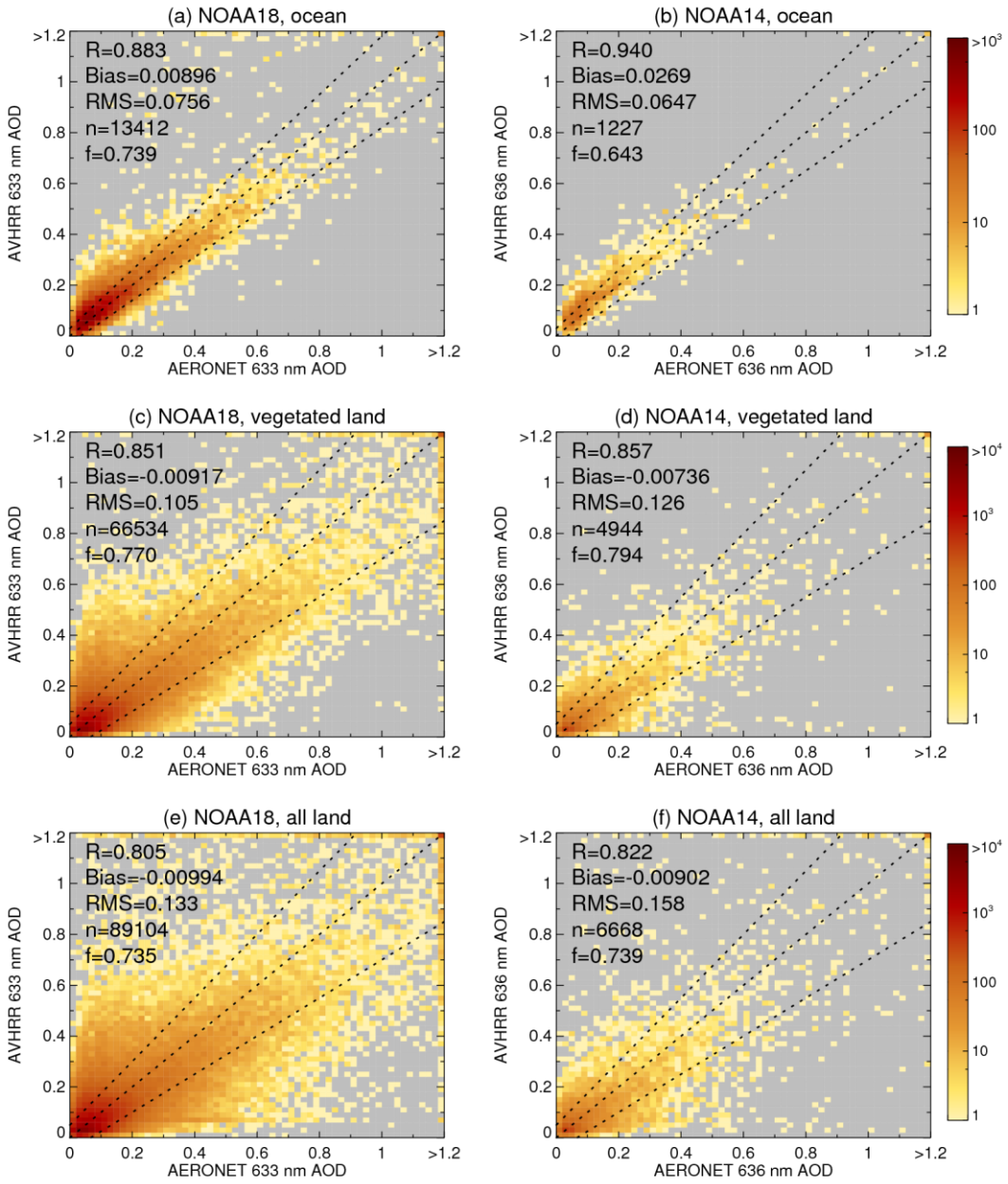

1041

1042 Figure 15. Scatter density histograms between AERONET and AVHRR AOD at band 1. Data
1043 are shown separately for (a, c, e) NOAA18 and (b, d, f) NOAA14, for (a, b) SOAR ocean
1044 retrievals, (c, d) Deep Blue land retrievals for vegetated scenes, and (e, f) all Deep Blue land
1045 retrievals. Dashed lines indicate the expected error (EE) envelopes of ±(0.03+15%) over water
1046 and ±(0.05+25%) over land, respectively. Statistics indicate the correlation coefficient (R),

1047 median (AVHRR-AERONET) bias, root mean square (RMS) error, data count (n), and fraction
1048 of points matching within the EE (*f*).
1049
1050